SEARCH FOR RESONANT DOUBLE HIGGS PRODUCTION WITH BBZZ DECAYS IN THE $b\bar{b}\ell\ell\nu\bar{\nu}$ FINAL STATE IN pp COLLISIONS AT $\sqrt{s} = 13$ TeV

by

Rami Kamalieddin

A DISSERTATION

Presented to the Faculty of

The Graduate College at the University of Nebraska

In Partial Fulfilment of Requirements

For the Degree of Doctor of Philosophy

Major: Physics and Astronomy

Under the Supervision of Professor Ilya Kravchenko

Lincoln, Nebraska

May, 2019

SEARCH FOR RESONANT DOUBLE HIGGS PRODUCTION WITH BBZZ DECAYS IN THE $b\bar{b}\ell\ell\nu\bar{\nu}$ FINAL STATE IN pp COLLISIONS AT $\sqrt{s} = 13$ TeV

Rami Kamalieddin, Ph.D.

University of Nebraska, 2019

Advisers: Ilya Kravchenko

Since the discovery of the Higgs boson in 2012 by the A Toroidal LHC ApparatuS (ATLAS) and The Compact Muon Solenoid (CMS), most of the quantum mechanical properties that describe the long-awaited Higgs boson have been measured. Due to an impeccable work of the LHC, dozens of fb^{-1} of data have been delivered to both experiments. Finally, it became possible for analyses that have a very low cross section to observe rare decay modes of the Higgs boson, as was done successfully recently in ttH and VHbb channels. The only untouched territory is a double Higgs boson production. Data will not help us much either at the HL-LHC, the process will remain unseen even in the most optimistic scenarios, so one has to rely solely on new reconstruction methods as well as new analysis techniques. This thesis is addressing both goals. I have been blessed by an opportunity to work in the CMS electron identification group, where we have developed new electron identification algorithms. The majority of this thesis, however, will be devoted to the second goal of HL-LHC. We establish the techniques for the first ever analysis at the LHC that searches for the double Higgs production mediated by a heavy narrow-width resonance in the $b\bar{b}ZZ$ channel: $X \to HH \to b\bar{b}ZZ^{*} \to b\bar{b}\ell\ell\nu\bar{\nu}$. The analysis searches for a resonant production of a Higgs boson pair in the range of masses of the resonant parent particle from 250 to 1000 GeV. Both spin scenarios of the resonance are considered: spin 0 (later called "graviton") and spin 2 (later called "radion"). In the absence of the

evidence of the resonant double Higgs boson production from the previous searches, we set upper confidence limits. When combined with other search channels, this analysis will contribute to the discovery of the double Higgs production and we would be able to finally probe the Higgs boson potential using its self-coupling.

"... a place for a smart quote!"

Lenin, 1922.

ACKNOWLEDGMENTS

This will be a longgggg list!

Table of Contents

List of Figures viii

List of Tables xii

1 Analysis overview **1**

1.1 Analysis Strategy 2

2 Data and Triggers **4**

2.1 Data 4

2.2 Triggers 5

3 Simulated Samples **13**

3.1 Signal simulation 13

3.2 Background simulation 14

4 Physics Objects Reconstruction **17**

4.1 Electrons 17

4.2 Muons 18

4.3 Jets 19

4.4 Identification of b jets 20

4.5 Missing transverse energy 20

5 Event Selection **22**

5.1 Higgs and Z Boson Selection 22

5.2 H $\rightarrow b\bar{b}$ and Z $\rightarrow \ell\ell$ variables to define signal and control regions . . . 26

5.3 Signal and background characteristics 27

5.4 Data and MC comparison 29

5.5 Scale Factors 31

6 BDT Discriminant **33**

6.1 Construction of the BDT 33

7 Systematic Uncertainties **49**

7.1 Normalization uncertainties 49

7.2 Shape uncertainties 51

8 Statistical Analysis **54**

9 Limits Extraction **57**

9.1 Optimization for the best limit 57

9.2 Results from the fit 58

10 $bbZZ$ measurements and combination of all HH channels **64**

Bibliography **66**

References **66**

List of Figures

1.1 The Feynman diagram of the graviton/radion production with the subsequent decay to HH. HH system decays to a pair of b quarks and Z bosons. Shown is 2 b quarks, 2 leptons, and 2 neutrinos final state. 2

2.1 Electron scale factors in p_T and η bins for 2016 data set for the HLT_Ele23_Ele12_CaloIdL_Tr trigger. ID cut (general purpose MVA WP90) and ISO cuts are applied, then the scale factors are measured. Taken from [1] 7

2.2 Muon scale factors in p_T and η bins for 2016 data runs B, C, D, E, F, G for the HLT_Mu17_TrkIsoVVL_Mu8_TrkIsoVVL_v* OR HLT_Mu17_TrkIsoVVL_TkMu8_T oVVL_v* triggers. Left: Scale factors for 8 GeV leg. Right: Scale factors for 17 GeV leg, provided that the subleading leg passed 8 GeV cut. . . . 8

2.3 Muon scale factors in p_T and η bins for 2016 data run H for the HLT_Mu17_TrkIsoVVL_Mu8_ OR HLT_Mu17_TrkIsoVVL_TkMu8_TrkIs oVVL_v* triggers. Left: Scale factors for 8 GeV leg. Right: Scale factors for 17 GeV leg, provided that the subleading leg passed 8 GeV cut. 8

2.4 Scale factors in η bins of the leading and subleading muons for 2016 data set for dZ requirement, measured after muons have passed the HLT_Mu17_TrkIsoVVL_Mu8_ OR HLT_Mu17_TrkIsoVVL_TkMu8_TrkIsoVVL_v* triggers. 9

2.5 Muon ID scale factors in p_T and η bins. Left: runs B to F. Right: runs G and H. 10
2.6 Muon ISO scale factors in p_T and η bins. Left: runs B to F. Right: runs G and H. 11
2.7 Electron ID+ISO scale factors in p_T and η bins. 12

4.1 Z boson (left) and photon (right) kinematics with the vector of all the visible objects (denoted by u) and a resulting MET. 21

5.1 Significance-like ($\sqrt{S}/B$) figure of merit as a function of the MET cut. Green curve shows the significance for our analysis keepings event above the cut, red curve is for HIG-18-013 analysis and their phase space is below the cut value. Top: 300 GeV cut. Middle: 600 GeV cut. Bottom: 900 GeV cut. On the left dielectron channel is shown, while dimuon plots are on the right. 25
5.2 Signal region, control region $t\bar{t}$, and control region Drell-Yan in the phase space of $\mathrm{Z} \to \ell\ell$ and $\mathrm{H} \to b\bar{b}$ masses. 26
5.3 Cut flow for mm (top) and ee (bottom) channels. 30
5.4 Transverse mass of the reconstructed HH candidates for data, the simulated signal graviton sample for the 300 GeV mass hypothesis, and simulated backgrounds scaled according to the fit results. The top row shows the figures for the muon channel while the bottom row is for the electron channel. For each row, the left plot is for the Drell-Yan control region, the middle is for the $t\bar{t}$ control region, and the right is for the signal region. Signal normalization choice is discussed in the text. The crosshatched area represents the sum of statistical and systematic uncertainties. 31

5.5 Transverse mass of the reconstructed HH candidates for data, the simulated signal radion sample for the 300 GeV mass hypothesis, and simulated backgrounds scaled according to the fit results. The top row shows the figures for the muon channel while the bottom row is for the electron channel. For each row, the left plot is for the Drell-Yan control region, the middle is for the $t\bar{t}$ control region, and the right is for the signal region. Signal normalization choice is discussed in the text. The crosshatched area represents the sum of statistical and systematic uncertainties. 32

6.1 Ranking of variables in the BDT training for electron(muon) channel at the top(bottom). Left: low mass BDT. Right: high mass BDT. 34

6.2 BDT plots for radion case, electron(muon) channel at the top(bottom). Signal region, 300 GeV mass hypothesis. For electrons cut is at 0.4, for muons at 0.7. More details at the table 9.1. 35

6.3 Variables used in the low mass training for electron channel. Index '1' refers to $b\bar{b}$ and index '0' refers to ZZ. 36

6.4 Variables used in the high mass training for electron channel. 37

6.5 BDT discriminants for electron channel. Top: low mass training. Bottom: high mass training. 39

6.6 ROC curves for electron channel. Top: low mass training. Bottom: high mass training. 40

6.7 Input variables correlations for electron channel, low mass training. Top: signal sample mix. Bottom: background sample mix. 41

6.8 Input variables correlations for electron channel, high mass training. Top: signal sample mix. Bottom: background sample mix. 42

6.9 Variables used in the low mass training for muon channel. Index '1' refers to $b\bar{b}$ and index '0' refers to ZZ. 43
6.10 Variables used in the high mass training for muon channel. 44
6.11 BDT discriminants for muon channel. Top: low mass training. Bottom: high mass training. 45
6.12 ROC curves for muon channel. Top: low mass training. Bottom: high mass training. 46
6.13 Input variables correlations for muon channel, low mass training. Top: signal sample mix. Bottom: background sample mix. 47
6.14 Input variables correlations for muon channel, high mass training. Top: signal sample mix. Bottom: background sample mix. 48

9.1 Cut on the BDT output vs 'r-value' from Combine. Electron channel. . . 61
9.2 Cut on the BDT output vs 'r-value' from Combine. Muon channel. . . . 62
9.3 Expected (dashed line) and observed (solid line) limits on the cross section of a resonant HH production as a function of the mass of the narrow resonance for both leptonic channels combined. Graviton case is shown at the top and radion case at the bottom. The red line shows a theoretical prediction for the production of a WED particle with certain model assumptions [2]. 63

10.1 Combination of HH channels using 2016 data. Expected (dashed) and observed (solid line) 95% CL exclusion limits are shown. The results describe the production cross section of a narrow width spin 0 (top) and spin 2 (bottom) resonance decaying into a pair of SM Higgs bosons. . . 65

List of Tables

2.1 List of used 2016 DoubleMuon data sets. An uncertainty of 2.5% is assigned for the 2016 data set luminosity [3] 4

2.2 Triggers for dimuon and dielectron analysis channels both at L1 and HLT levels. 5

3.1 Background Monte Carlo samples 15

5.1 $\not{E}_{\mathrm{T}}$ cut to orthogonalise the analysis with respect to HIG-18-013. 24

5.2 Efficiency of the BDT selection requirement. ee channel (top) and $\mu\mu$ channel (bottom). 27

5.3 Number of events surviving analysis cuts corresponding to the last entry in the 5.3 29

9.1 Suboptimal BDT cuts used in the analysis 58

9.2 The expected and observed HH production cross section upper limits at 95% CL for different narrow resonance graviton (top) and radion (bottom) mass hypotheses for both dielectron and dimuon channels combined. . . 60

Chapter *1*

Analysis overview

In 2012, CMS [4] and ATLAS [5] collaborations officially discovered a Higgs-like particle and with that breakthrough the picture of the SM [6–8] of the particle physics has been completed. Most of the basic properties of the Higgs boson have been measured. However, it remains difficult to distinguish several processes with very low cross sections from the irreducible SM background processes with a similar signature. One such important but rare process is a double Higgs (HH) boson production. HH directly relates to the Higgs boson self-coupling, and thus, has an access to the shape of the Higgs boson potential. In the SM, HH production is a non-resonant process with a cross section of $\sigma =$ fb [9] at $\sqrt{s} = 13$ TeV.

Several Beyond the Standard Model (BSM) theories and models, such as supersymmetry, composite Higgs, Warped Extra Dimensions (WED) [2, 10–13], predict scenarios when the double Higgs boson cross section is significantly increased and may be observed with the current data. There may be two different types of the BSM HH production: a non-resonant production, introducing BSM terms to the SM lagrangian or a resonant production, in which the process is mediated by a narrow width heavy mass resonance that subsequently would decay to SM Higgs bosons. [13].

In this analysis through the gluon fusion mechanism a heavy narrow resonance, such as RS1 KK graviton or RS1 radion ("graviton" or "radion" later in the text) [14–16] is produced. It decays to two Higgs bosons, which further decay to the bb pair (the first Higgs boson) and the ZZ/WW pair (the other Higgs boson). The analysis covers masses of graviton/radion from 250 GeV to 1000 GeV. Since no evidence of the signal has been reported by the previous HH analyses, we proceed directly to setting 95 % upper confidence limits on the production of the graviton with a subsequent decay to Higgs bosons times the branching ratios of the Higgs boson decaying to a pair of b quarks and the other Higgs boson to two leptons and two neutrinos respectively (Fig. 1.1). We observe no deviation with the given data and evaluated uncertainties, the results are compatible with the Standard Model.

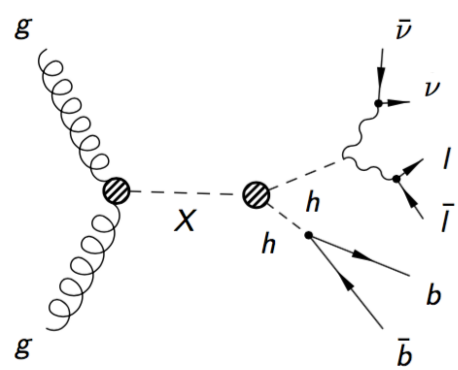

Figure 1.1: The Feynman diagram of the graviton/radion production with the subsequent decay to HH. HH system decays to a pair of b quarks and Z bosons. Shown is 2 b quarks, 2 leptons, and 2 neutrinos final state.

1.1 Analysis Strategy

The analysis is based on ntuples and object selection from the approved VHbb sister analysis [17]. Leptons, b jets, and the missing transverse energy (MET) are reconstructed using the standard CMS procedures [18] and the Particle Flow (PF) algorithm [19]. b-jets are identified using the Combined MVA v2 (CMVA) algorithm [20]. Then, on shell Z boson candidates are selected of dilepton pairs of the same flavour with a net charge zero for a pair. Higgs boson candidate decaying to b quarks (Hbb) is reconstructed as a pair of b jets with the highest CMVA output value. Finally, double Higgs boson pseudo-transverse mass, which is used in the shape analysis to extract limits, is constructed computing the transverse mass of the sum of the Lorentz vectors of the two leptons forming the on-shell Z, MET, and a pair of the b jets forming the H $\to b\bar{b}$. Additionally, a cut on the missing transverse energy is introduced to preserves the orthogonality with the existing HIG-18-013 “2b 2l 2q” analysis, which also works with the $bbZZ$ decays. In a similar fashion, the cut on the Z mass ($m_Z > 76$ GeV) is used to orthogonalise the analysis with respect to the HH phase space used in the legacy $bbWW$ analysis where the final signature is identical to ours. Lastly, the cut on the BDT is used to reduce the background contamination in the signal region.

Main backgrounds are $t\bar{t}$ and Drell-Yan in association with jets. To determine their normalization, we construct two dedicated control region, which are correspondingly $t\bar{t}$ and Drell-Yan dominated. Then, during the the simultaneous fit of signal region (SR), as well as control region $t\bar{t}$ (CRTT), and control region Drell-Yan (CRDY), we obtain rates for these processes. Others, minor backgrounds, are single top production, diboson samples (WW, WZ, ZZ), and ZH production and are determined from the Monte Carlo (MC) simulation.

In the next chapters we will discuss all of the aspects of the analysis in details starting with the chapter on Data.

Chapter 2

Data and Triggers

2.1 Data

This measurement uses the full dataset of 2016 collected with the CMS detector in pp collisions at 13 TeV center-of-mass energy with the corresponding integrated luminocity of 35.9 fb^{-1}.

As the measurement is based on dilepton signatures, the DoubleMuon and DoubleElectron primary datasets are analyzed and only on-shell $Z(\ell\ell)$ decays are considered, where $\ell = \mathrm{e}, \mu$. CMS delivered data in several runs. The run periods and the corresponding integrated luminosities are listed in Table 2.1 for DoubleMuon channel, DoubleElectron channel numbers are similar.

Table 2.1: List of used 2016 DoubleMuon data sets. An uncertainty of 2.5% is assigned for the 2016 data set luminosity [3]

Dataset	$\int \mathcal{L}$ (fb^{-1})
DoubleMuon__Run2016B-03Feb2017-v2	$\sim$5.9
DoubleMuon__Run2016C-03Feb2017-v1	$\sim$2.7
DoubleMuon__Run2016D-03Feb2017-v1	$\sim$4.3
DoubleMuon__Run2016E-03Feb2017-v1	$\sim$4.1
DoubleMuon__Run2016F-03Feb2017-v1	$\sim$3.2
DoubleMuon__Run2016G-03Feb2017-v1	$\sim$3.8
DoubleMuon__Run2016H-03Feb2017-v1	$\sim$11.8
Total Lumi	35.9

2.2 Triggers

The rate at which particles are produced at LHC is not suitable for a direct persistence to the tape, it is too high and contains lots of uninteresting events. Therefore, we need a "trigger" that can select the potentially interesting events, such as those which will produce the Higgs particle or a Z/W boson, etc. In parallel, trigger also reduces the rate to just a few hundred "events" per second, which can be read out and stored on computer disk for subsequent offline analysis. Our $bbZZ$ analysis is performed in the dielectron and dimuon channels, so low momentum events are important to us. That is why unprescaled dilepton triggers with the lowest available transverse momentum thresholds are utilised. The triggers at the level 1 (L1) and high level trigger (HLT) are listed in Table 2.2. Dielectron trigger requires the leading electron to pass 23 GeV p_T cut and the trailing (subleading) electron to pass 12 GeV p_T cut, both electrons should be within $\eta < 2.5$. Dimuon triggers require the leading muon to pass 17 GeV p_T cut and 8 GeV p_T cut for the subleading muon, both muons should be within $\eta < 2.4$. The η region (1.4442 to 1.566) in the gap between the barrel and endcap is excluded.

Due to the fact that there are discrepancies between trigger efficiencies in data and in simulation, we need trigger scale factors. Before measuring them, identification

Table 2.2: Triggers for dimuon and dielectron analysis channels both at L1 and HLT levels.

Channel	L1 Seeds	HLT Paths
Z($\mu\mu$) Z($\nu\nu$)H $\rightarrow b\bar{b}$	L1_SingleMu20	HLT_Mu17_TrkIsoVVL_Mu8_TrkIsoVVL_v* OR HLT_Mu17_TrkIsoVVL_TkMu8_TrkIsoVVL_v* OR HLT_Mu17_TrkIsoVVL_Mu8_TrkIsoVVL_DZ_v* OR HLT_Mu17_TrkIsoVVL_TkMu8_TrkIsoVVL_DZ_v*
Z(ee) Z($\nu\nu$)H $\rightarrow b\bar{b}$	L1_SingleEG30 OR L1_SingleIsoEG22er OR L1_SingleIsoEG24 OR L1_DoubleEG_15_10	HLT_Ele23_Ele12_CaloIdL_TrackIdL_IsoVL_DZ

(ID) and isolation (ISO) cuts should be applied. Identification criteria helps selecting real prompt leptons, which isolation criteria stresses the fact that a track for the real prompt lepton should be isolated from the other activity nearby. Further, p_T cuts of the offline selection are replicated. For dielectron trigger leading and subleading electrons have to pass 25 GeV p_T cut and 15 GeV p_T cut correspondinly. Dimuon triggers require the leading muon to pass 20 GeV p_T cut and 15 GeV p_T cut for the subleading muon. Dilepton scale factor have been computed for each leg separately, since the cuts on each leg vary (Fig. 2.1). Following the recommendations from the Muon Particle Object Group (POG), scale factors have been computed separately for two groups: run H and other runs, and then the final scale factors are determined as luminosity averaged scale factors (Figs. 2.2, 2.3, 2.4). Muon ID, ISO, and electron ID+ISO scale factors are shown at Figs. 2.5, 2.6, 2.7.

Leg 1

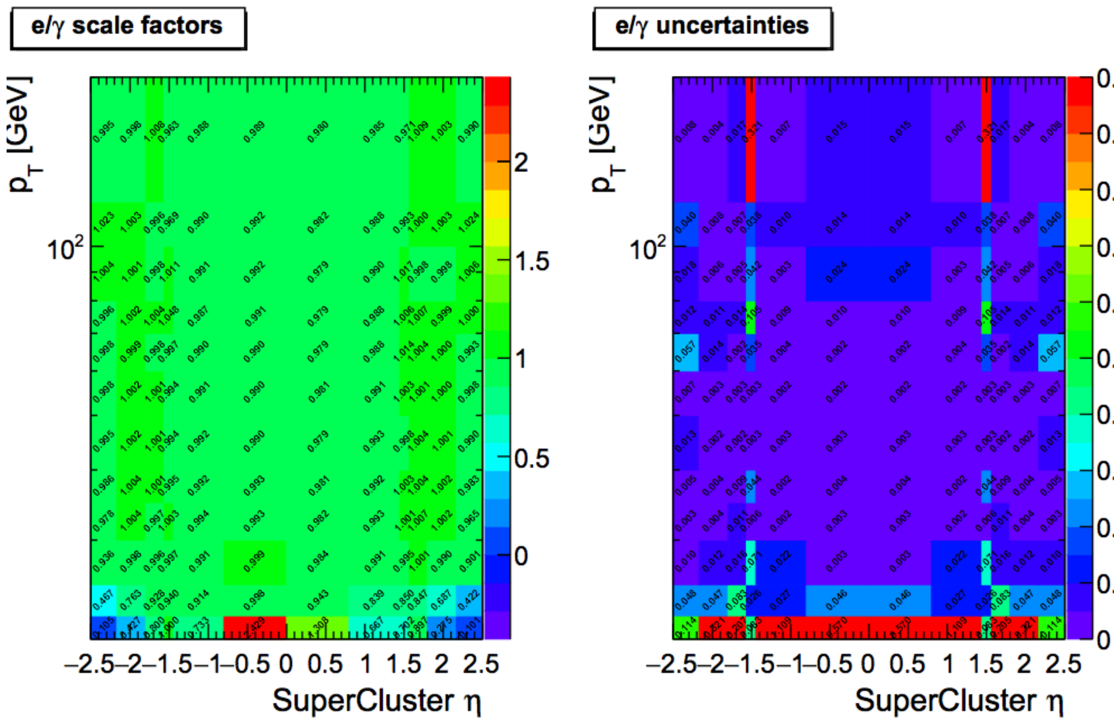

Leg 2

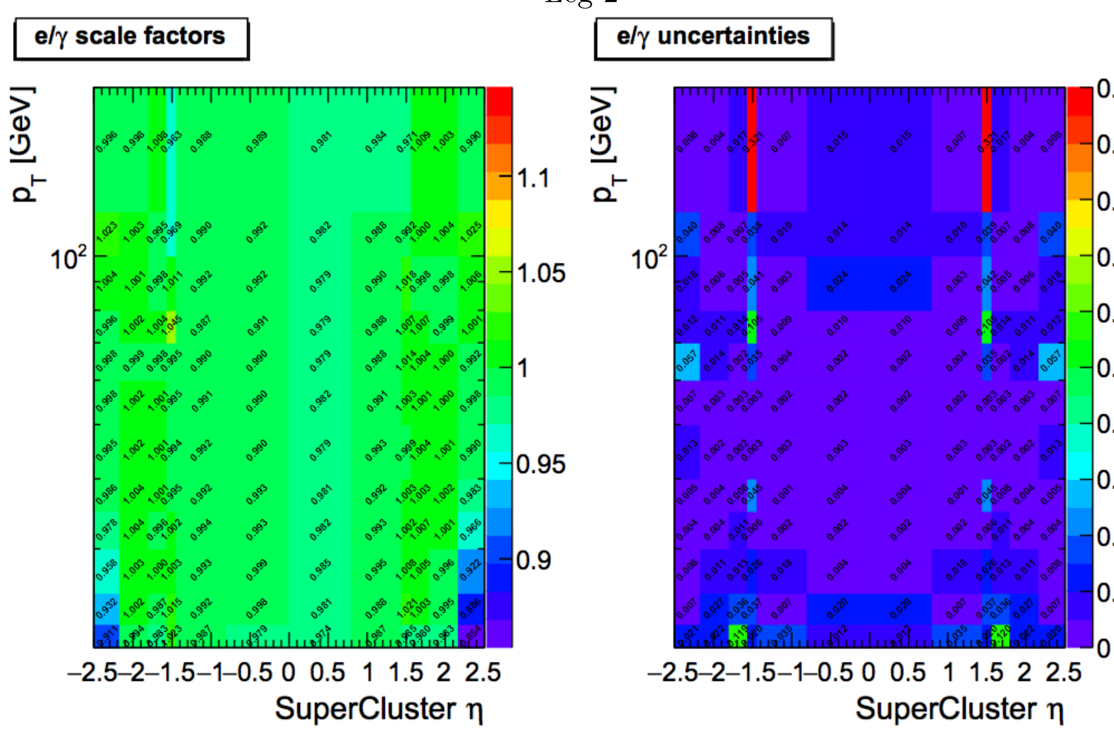

Figure 2.1: Electron scale factors in p_T and η bins for 2016 data set for the HLT_Ele23_Ele12_CaloIdL_TrackIdL_IsoVL_DZ trigger. ID cut (general purpose MVA WP90) and ISO cuts are applied, then the scale factors are measured. Taken from [1]

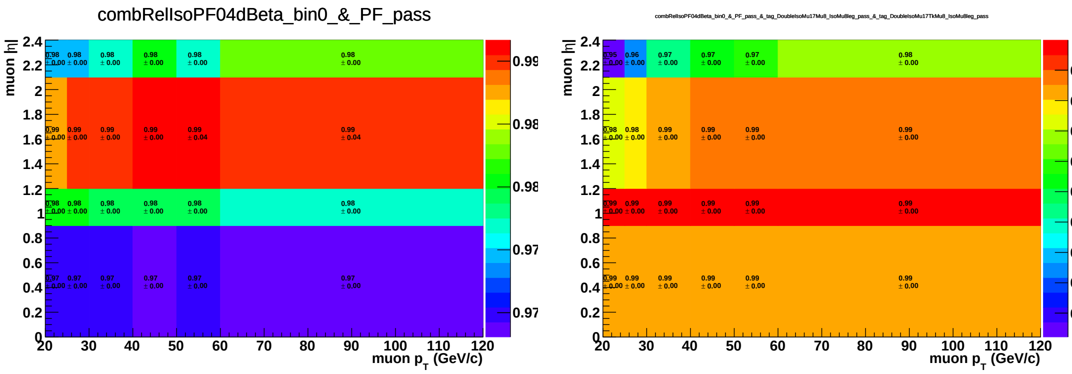

Figure 2.2: Muon scale factors in p_T and η bins for 2016 data runs B, C, D, E, F, G for the HLT_Mu17_TrkIsoVVL_Mu8_TrkIsoVVL_v* OR HLT_Mu17_TrkIsoVVL_TkMu8_TrkIs oVVL_v* triggers. Left: Scale factors for 8 GeV leg. Right: Scale factors for 17 GeV leg, provided that the subleading leg passed 8 GeV cut.

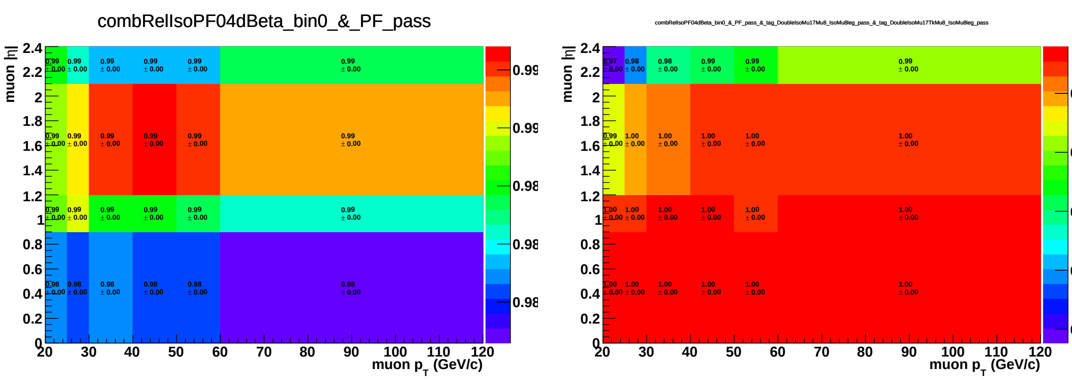

Figure 2.3: Muon scale factors in p_T and η bins for 2016 data run H for the HLT_Mu17_TrkIsoVVL_Mu8_TrkIsoVVL_v* OR HLT_Mu17_TrkIsoVVL_TkMu8_TrkIs oVVL_v* triggers. Left: Scale factors for 8 GeV leg. Right: Scale factors for 17 GeV leg, provided that the subleading leg passed 8 GeV cut.

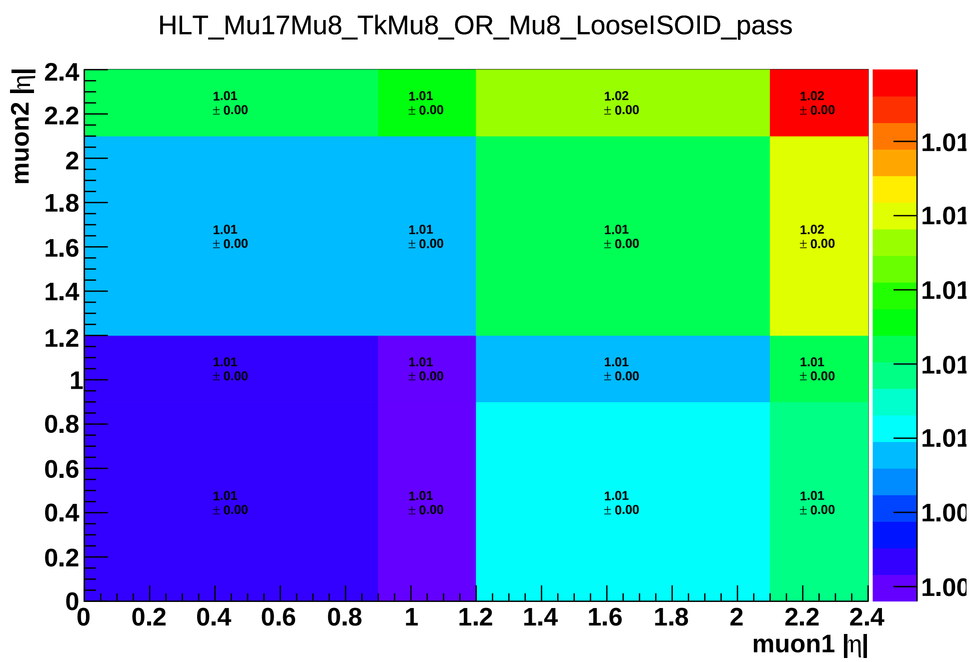

Figure 2.4: Scale factors in η bins of the leading and subleading muons for 2016 data set for dZ requirement, measured after muons have passed the HLT_Mu17_TrkIsoVVL_Mu8_TrkIsoVVL_v* OR HLT_Mu17_TrkIsoVVL_TkMu8_TrkIsoVVL_v* triggers.

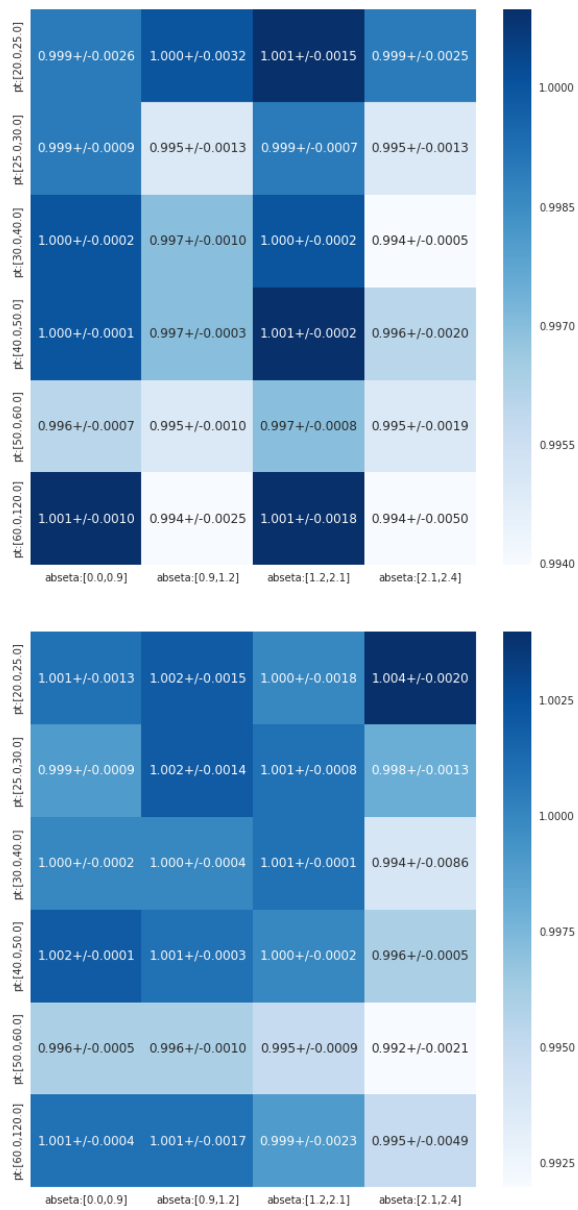

Figure 2.5: Muon ID scale factors in p_T and η bins. Left: runs B to F. Right: runs G and H.

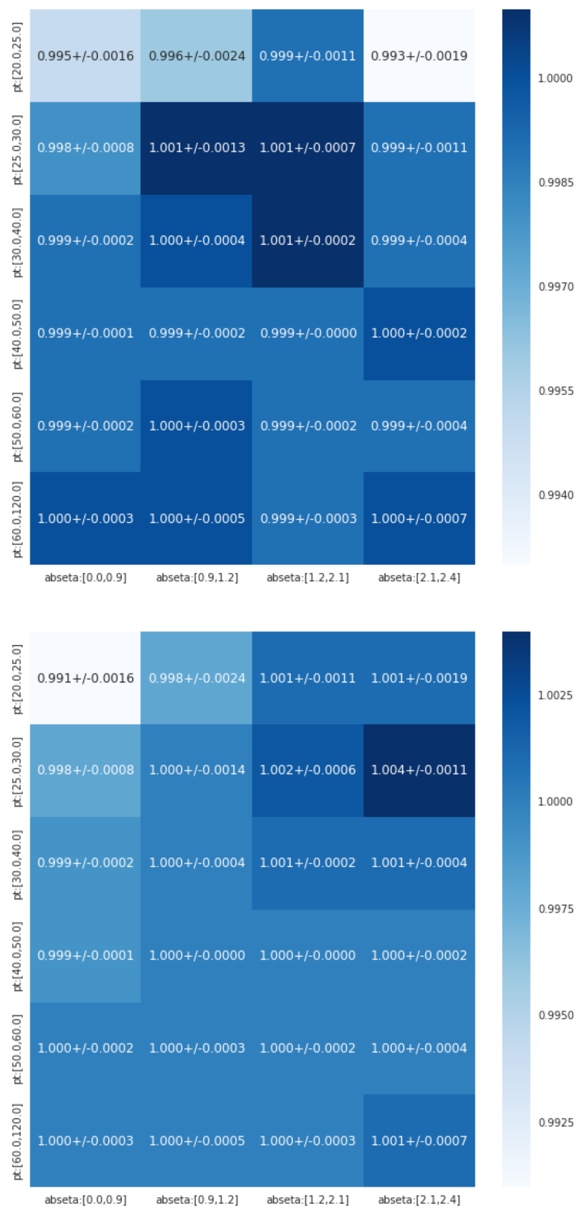

Figure 2.6: Muon ISO scale factors in p_T and η bins. Left: runs B to F. Right: runs G and H.

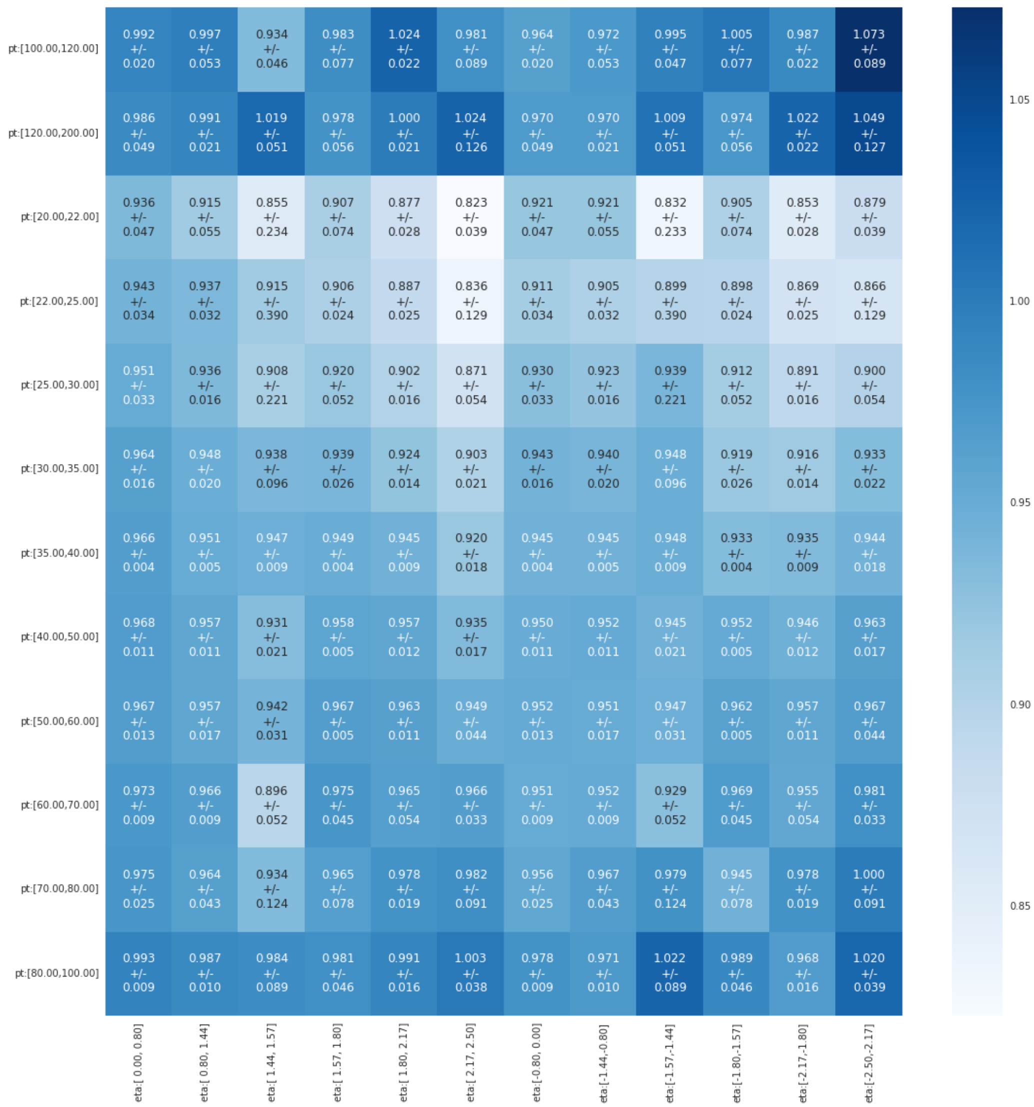

Figure 2.7: Electron ID+ISO scale factors in p_T and η bins.

Chapter 3

Simulated Samples

Before we look at the data, all the studies are done with the simulation. The most important requirements on the simulation is that it is accurate and has enough events in all the phase space corners. While this is almost true for the main backgrounds, for which the simulated samples are produced centrally for the use of the whole CMS, specific signal samples cannot be produced with big statistics for all analyses, since there are hundred analysis teams in CMC. Luckily for us, both $bbZZ$ and $bbWW$ samples have been produced with O(0.5 M events).

3.1 Signal simulation

MC signal samples of the resonant Higgs boson pair production have been generated at the Leading Order (LO) using the MadGraph 5 version 2.2.2.0 generator [21]. The gluon fusion production of a heavy narrow resonance is followed by the decay of the resonance into two SM Higgs bosons whose mass is fixed at 125 GeV.

Two signal MC samples are generated to cover the Higgs decay modes contributing to the 2 b jets 2 leptons 2 neutrinos final state of this measurement. The first sample type is a HH decay in to bbZZ channel, where one Higgs boson decays to a pair of b-quarks and the second Higgs boson decays into two Z bosons. In the second sample type bbVV events are generated, where HH can decay through bbWW and bbZZ channels. For both samples, the Z boson-pair and the W boson-pair are set to decay leptonically to two leptons and two neutrinos, where a lepton could be an electron or a muon. The second, bbVV, sample is filtered using the generator level information such that only the events with a W-boson pair (bbWW) are kept, while the Z-pair events are dropped: there are very few of them in the bbVV sample, and most importantly, high statistics bbZZ is taken from the dedicated bbZZ sample of the first type.

Events in the signal bbZZ and bbWW MC samples are normalised to 2 pb HH production cross section, which is a typical value of the heavy resonance production at 300 GeV predicted by the WED. Additionally the normalization includes the branching ratios of the Higgs boson decays contributing to the final state studied here: 0.0012 and 0.0266 for $HH \to bbZZ \to bb\ell\ell\nu\nu$ and $HH \to bbWW \to bb\ell\nu\ell\nu$, respectively [22].

Unless mentioned otherwise, throughout the text plots and numbers represent the graviton study. The data and backgrounds for the radion measurement are the same, thus distributions also show the same good Data MC agreement and can be found for at Figs. 5.4 for the graviton case and 5.5 for the radion case.

3.2 Background simulation

In this analysis the main backgrounds are $t\bar{t}$ and Drell-Yan plus jets with the mass of the boson greater than 50 GeV. Not all the background processes pass our tight preselection (see section 5), those which do, are single top, dibosons, and ZH backgrounds that are listed in the Table 3.1:

The simulated samples of the background processes such as $t\bar{t}$ [23] and the single

Table 3.1: Background Monte Carlo samples

DY1JetsToLL_M-50_TuneCUETP8M1_13TeV-madgraphMLM-pythia8
DY2JetsToLL_M-50_TuneCUETP8M1_13TeV-madgraphMLM-pythia8
DY3JetsToLL_M-50_TuneCUETP8M1_13TeV-madgraphMLM-pythia8
DY4JetsToLL_M-50_TuneCUETP8M1_13TeV-madgraphMLM-pythia8
WW_TuneCUETP8M1_13TeV-pythia8
WZ_TuneCUETP8M1_13TeV-pythia8
ZZ_TuneCUETP8M1_13TeV-pythia8
ZH_HToBB_ZToLL_M125_13TeV_aMC@NLO
TT_TuneCUETP8M1_13TeV-powheg-pythia8
ST_tW_top_5f_inclusiveDecays_13TeV-powheg-pythia8_TuneCUETP8M1
ST_tW_antitop_5f_inclusiveDecays_13TeV-powheg-pythia8_TuneCUETP8M1
ST_t-channel_top_4f_leptonDecays_13TeV-powheg-pythia8
ST_t-channel_antitop_4f_leptonDecays_13TeV-powheg-pythia8
ST_s-channel_4f_leptonDecays_13TeV-amcatnlo-pythia8

top tW and t-channel production processes [24] are generated at the next-to-leading order (NLO) with POWHEG [25], while single top s-channel production process is generated at NLO with MadGraph. $t\bar{t}$ and single top production cross sections are rescaled to the next-to-next-to-leading order (NNLO). Drell-Yan (DY) process samples in association with 1, 2, 3 or 4 jets are generated at the leading order using MadGraph with the MLM matching [26] and rescaled to NNLO using fewz program [27–29].

As for the electroweak (EWK) order, DY samples have been rescaled to EWK NLO order with the NLO/LO k-factor of 1.23 [30]. Diboson samples are generated at LO with pythia8.212 [31].

The main background process, which involves SM Higgs boson, is an associated production of the Higgs boson with a Z boson (ZH). ZH process is simultated using the generator $MadGraph5\_aMC@NLO$ [32] with FxFx merging [33] and rescaled to NNLO with mcfm generator [34].

For LO and NLO samples NNPDF3.0 parton distribution functions (PDF) set is used. POWHEG and MadGraph interfaced with PYTHIA8.212 [31] are used for the parton showering and hadronization steps. To describe the underlying event CUETP9M1 set derived in [35] is used. Geant4 [36] is used to model the response of the CMS detector.

All the final cross sections denoted as NNLO are calculated at NNLO QCD accuracies and have been computed with the tool they were generated with. They found to be in agreement with the values from the LHC Higgs cross section working group [37–41].

During the data taking in 2016 the average number of proton-proton interactions per bunch crossing was 24 (denoted as pile up later), and in MC samples this information has been introduced overlapping these interactions with the events of interest.

Chapter 4

Physics Objects Reconstruction

This the first ever bbZZ analysis performed at CERN with the real data. We use the standard set of the CMS reconstructed physics objects. Below, we describe reconstruction of each separately: electrons, muons, jets and b jets, and MET.

4.1 Electrons

The Gaussian Sum Filter (GSF) algorithm is used to reconstruct electrons [42]. GSF helps to estimate track parameters. The procedure starts as follows: a mixture of Gaussian distributions (normally about 4-6 components) [43] is used to estimate the energy loss in each layer of the tracker. The energy loss is modelled by the Bethe-Heitler formula. Two most important track properties are then computed: a weighted mean and the most frequent value (mode). The first estimate is unbiased while the latter one has a smaller width. In practice, mostly one works with the mode. Gaussian mixtures are determined minimising either the absolute difference between the cumulative density functions (CDFs) of the model and of the Gaussian mixture, or the Kullback-Leibner distance, which is a logarithm of the ratio of the probability density functions (pdfs) of the model with respect to the mixture. Finally, the tracks are extrapolated further to the ECAL The measurement selects electrons, which pass the following selection: leading electron $p_{\mathrm{T}} > 25\,\mathrm{GeV}$ and subleading electron $p_{\mathrm{T}} > 15\,\mathrm{GeV}$, $|\eta| < 2.5$, an isolation cut of 0.06, for which the cone of 0.3 is used to compute the ρ-subtracted PF isolation. Lepton isolation is calculated as a scalar sum of the transverse momentum (p_T) of all the charged and neutral hadrons as well as photons around the lepton (excluding the cone) normalised to the p_T of the lepton itself.

On top of the selection defined above, a specific CMS Particle Object Group (POG) recommended working point (WP) is applied, which is a discriminant based on the a multivariate analysis (MVA) for classification of signal/background electrons. The WP consists of nearly 20 variables utilising the information from the impact point, tracks, and the ECAL: χ^2 variables of the track and the quality of its estimate, $\delta\eta$, $\delta\phi$, energy of the 3 by 3 cluster, ECAL energy over momentum, etc. For this analysis we use the loose working point (another name can be WP90), as described in [1]. ID and ISO, as well as the HLT SFs are applied.

4.2 Muons

In this analysis we are using global muons reconstructed using the information from the tracker and muon system [44,45]. During the offline reconstruction, muons chambers segments are used as seeds for the "standalone muon" reconstruction. The seed is a position, a direction, and an initial momentum of the muon candidate. This serves as an input to the track fitting procedure utilising muon system information. The resulting object after executing this technique is what is called a standalone muon. Then, for each standalone muon the algorithm searches for the tracks reconstructed in the inner tracking system (tracker tracks) that would match the muon. Then for each standalone muon - tracker track pair the Kalman filter based fit [46] is performed.

The result is a collection of muons which are referred to as global muons. In this analysis the kinematic and isolation selection of global muons is the following: leading muon $p_{\mathrm{T}} > 20\,\mathrm{GeV}$ and subleading muon $p_{\mathrm{T}} > 15\,\mathrm{GeV}$, $|\eta| < 2.4$, a relative isolation cut of 0.15, with the cone of 0.4 used to compute $\Delta\beta$-subtracted PF isolation. Finally, a tighter selection - muon POG recommended WP Loose is applied [44, 47]. WP consists of track quality information: χ^2 of various fits, number of good hits in the tracker, number of layer missing the expected hit, impact parameter variables, matching variables (e.g., a segment in the muon station matched to the tracker track extrapolation), compatibility variables (e.g., a muon segment compatibility). ID, ISO, HLT and tracker SFs are applied.

4.3 Jets

Particle flow (PF) algorithm is used to reconstruct jets [48, 49], with the help of the anti$-k_T$ clustering algorithm having a distance parameter of $R = 0.4$ [50,51]. Jets are collimated bunches of stable hadrons originating from quarks and gluons after fragmentation and hadronization. Therefore, jet finding procedure is a back-propagation that starts with the detected objects and following the rules of the quantum mechanics for fragmentation and hadronization targets to identify the initial partons. Anti $- k_T$ is a sequential clustering algorithm that first defines the notion of the distance between the two particles in the collection of particles of the event, and also a distance between the particle and the beam axis. Then sequentially iterating over the particles collection it computes the smallest distances, if the smallest one is between the particles, their 4-momentum is combined into one. If the smallest distance is between the particle and the beam axis, then the particle is called the jet, removed from the collection, and the whole procedure continues. anti $- k_T$ is known to be insensitive to the underlying event and to the pile up, therefore, is commonly used.

Reconstructed jets are further corrected for detector effects using specific corrections determined from the data and MC. Only jets passing $|\eta| < 2.4$ and ($p_{\mathrm{T}} > 30\,\mathrm{GeV}$) are considered for the analysis. All the necessary jet energy resolution (JER) and jet energy scale (JES) corrections provided by the JetMET group are applied [52].

4.4 Identification of b jets

MVA technique combining the information about the impact parameter, identified secondary vertices, as well as soft lepton (if any) contained inside of the jet is used by the CMVA algorithm to identify b quark originated jets. The output is a continuous MVA discriminant ranging in value from -1 to +1. Optimal cut is determined by the POG for several working points. We use CMVAv2 medium working point (> 0.4432). We checked all three WPs and WP Medium gives the best limits. b tagging and mistagging corrections are applied.

4.5 Missing transverse energy

Even though neutrinos leave no trace in the CMS detector, their presence may be inferred through the momentum imbalance. A quantity reconstructed in this fashion in the plane perpendicular to the beam axis is called a missing transverse energy/momentum (MET). Precise reconstruction of leptons, photons, jets, etc is necessary for the correct computation of the MET. Detector miscalibration and PU also affect MET performance, thus the studies with the real data are always conducted.

Due to the conservation of the momentum in the transverse plane, MET can be calculated as an absolute value of the negative vectorial sum of the transverse momentum of all observed particles: $\overrightarrow{E_T} \equiv -\sum \overrightarrow{p_T}$

MET reconstructed using PF reconstructed particles [53] is what the majority of the CMS teams uses for analyses of 2016 data. Several correction recommended by the JetMET POG are applied [54]: jet corrections, corrections for the PU effect, etc. On top, a set of filters related to the instrumental effects is employed, such as removal of the misreconstruction caused by the fisfier in the HCAL and/or noice in the tracker, etc. [55]. Schematic representation of the MET in the event with Z or photon is shown on the Fig. 4.1.

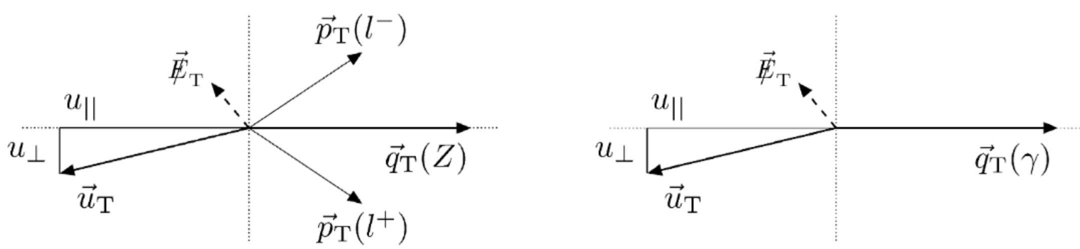

Figure 4.1: Z boson (left) and photon (right) kinematics with the vector of all the visible objects (denoted by u) and a resulting MET.

Chapter 5

Event Selection

The resonances in search decay to two SM Higgs bosons. However, Higgs bosons further decay almost immediately. Therefore, it is critical to reconstruct Higgs bosons decay products with the high precision.

5.1 Higgs and Z Boson Selection

Only dilepton pairs having net charge of zero are considered as $\mathrm{Z} \to \ell\ell$ candidates. Pairs of prompt isolated leptons must have a dilepton mass greater than 76 GeV. This ensures the orthogonality with HIG-17-006 bbVV analysis (later also referred to as bbWW analysis) as well as helps selecting decays of real Z bosons.

Higgs boson candidates are reconstructed from the b jet pairs utilising the two b jets with the highest CMVAv2 discriminant value. We do not veto additional b jets as with the increased PU growths the probability to have more b jets.

Double Higgs boson candidate is computed as a sum of Lorentz vectors of the $\mathrm{Z} \to \ell\ell$ candidate, MET, and a $\mathrm{H} \to b\bar{b}$ candidate. Then, we compute the transverse mass of that object.

This transverse mass definition that we follow is one of the commonly used and is logical in the sense that we subtract the longitudinal momentum component which leaves us with the transverse momentum components only (while the energy remains the total energy). More precisely, as the z-component of the neutrinos' momentum is unknown and we decided not to reconstruct it, we form a pseudo transverse mass: $\tilde{M}_T(HH) = \sqrt{E^2 - p_z^2}$ (further referred as transverse mass for brevity), where E and p_z are the energy and the z-axis component of the Lorentz energy-momentum vector of the HH candidate.

The resulting distribution, $\tilde{M}_T(HH)$, is what will be used in the binned shape analysis with the Higgs Combination Tool following the section "Binned shape analysis" as described at the twiki page [56]. Shape analysis is more sensitive than the simple cut-and-count experiment (one bin distributions) since more information/discrimination power is given to the likelihood function.

Initial data files, called ntuples, have enormous size of the order of more than a Terabyte per background process. To reduce the size of the ntuples and remove clear background events (on the other hand, to remove signal-like events we apply a sophisticated selection and use a BDT), we apply a "common-sense" HH preselection, which starts with the requirement on dilepton mass to be greater than 50 GeV and the event to contain at least two "good" jets - with $p_T > 30$ GeV and $|\eta| < 2.4$. In addition to requirements on Higgs bosons decaying to b quarks mentioned above, we define Z bosons as two opposite sign muons with $p_T > 20/15$ GeV (leading/subleading lepton) or two opposite sign electrons with $p_T > 25/15$ GeV (leading/subleading lepton).

Later analysis cuts, the selection chain to improve signal-background separation, include:

- the requirement of at least two b jets in the event, out of which two with the highest CMVAv2 score are used to define H $\rightarrow b\bar{b}$ candidate
- the lower end cut on the H $\rightarrow b\bar{b}$ mass set to 20 GeV to remove the low mass

resonances, while giving BDT as many events in the CRDY as possible at the same time. The upper end cut is not explicitly set for the same purpose. The actual H $\rightarrow b\bar{b}$ mass distribution after the analysis selection is concentrated in the range 30 to 220 GeV

- the Z boson selection takes the most energetic two leptons of the opposite sign and requires their dilepton mass to pass 76 GeV $<$ Z mass $<$ 106 GeV condition used for the signal region definition. This is a standard $\pm$ 15 GeV window for Z boson selection whose lower end also preserves othogonality with the existing HIG-17-006 bbVV analysis

- HH candidate is approximated by the sum of $\not{E}_{\mathrm{T}}$, Z, and H $\rightarrow b\bar{b}$ decays. A loose cut on HH transverse $>$ 100 GeV removes evidently background events

- finally, an additional set of $\not{E}_{\mathrm{T}}$ cuts is used to ensure orthogonality with the existing HIG-18-013 bbZZ analysis focusing on the 2b jets + 2 leptons + 2 quarks, see Table 5.1. The MET cuts have been optimised by both analyses to yield the best limit when the results of two measurements are combined.

Table 5.1: $\not{E}_{\mathrm{T}}$ cut to orthogonalise the analysis with respect to HIG-18-013.

Signal mass, GeV	$\not{E}_{\mathrm{T}}$ cut, GeV
260-300	$>$ 40
350-600	$>$ 75
650-1000	$>$ 100

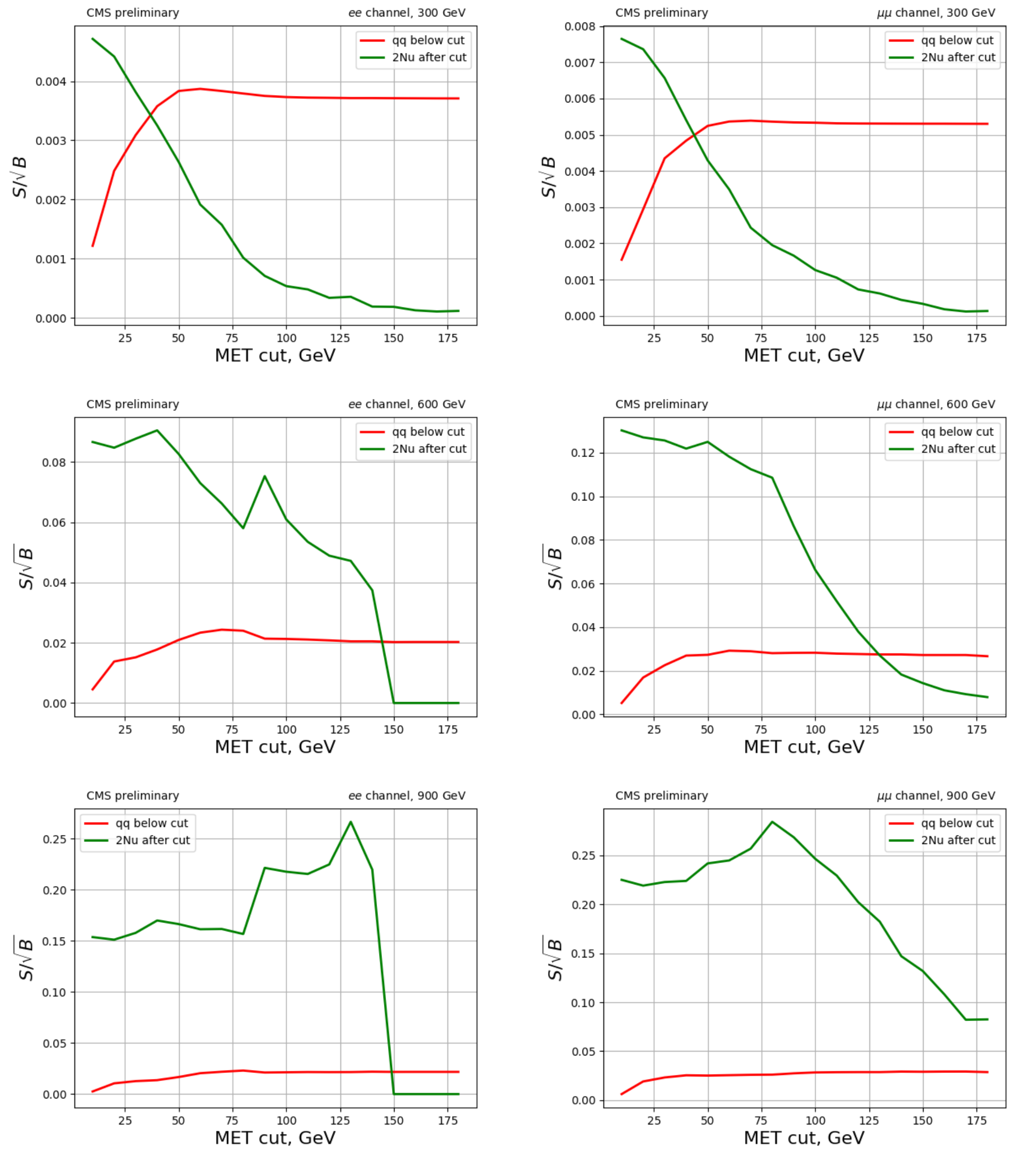

Figure 5.1: Significance-like ($\sqrt{S}/B$) figure of merit as a function of the MET cut. Green curve shows the significance for our analysis keepings event above the cut, red curve is for HIG-18-013 analysis and their phase space is below the cut value. Top: 300 GeV cut. Middle: 600 GeV cut. Bottom: 900 GeV cut. On the left dielectron channel is shown, while dimuon plots are on the right.

5.2 $\mathrm{H} \to b\bar{b}$ and $\mathrm{Z} \to \ell\ell$ variables to define signal and control regions

In this analysis we define three regions in the $\mathrm{H} \to b\bar{b}$ and $\mathrm{Z} \to \ell\ell$ space. Two regions, CRDY and CRTT, are used to extract the normalizations of DY and $t\bar{t}$ backgrounds correspondingly. Signal region (Fig. 5.2) is chosen by the set of $\mathrm{H} \to b\bar{b}$ and $\mathrm{Z} \to \ell\ell$ cuts 5.2. To further reduce background contamination in this region, an additional cut on the MVA output is used. Boosted decision trees (BDT) MVA technique is employed to separate background from signal. Below we describe in details selection of each region and BDT construction.

For CRDY we invert $\mathrm{H} \to b\bar{b}$ cut, keeping in the lower sideband only events with the mass of Higgs boson higher than 20 GeV to avoid fakes from QCD. For CRTT we invert $\mathrm{Z} \to \ell\ell$ cut, keeping only high mass sideband to ensure the orthogonality with the existing HIG-17-006 bbVV analysis, since the lower sideband is already included in the phase space used by them.

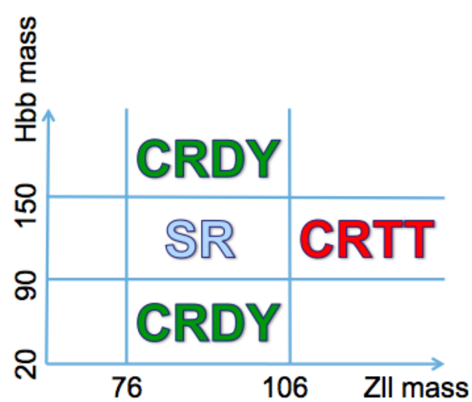

Figure 5.2: Signal region, control region $t\bar{t}$, and control region Drell-Yan in the phase space of $\mathrm{Z} \to \ell\ell$ and $\mathrm{H} \to b\bar{b}$ masses.

Table 5.2: Efficiency of the BDT selection requirement. ee channel (top) and $\mu\mu$ channel (bottom).

sample	Efficiency at 300 GeV, [%]	Efficiency at 900 GeV, [%]
signal (bbZZ)	89.2	94.9
signal (bbWW)	75.0	88.4
$t\bar{t}$	28.8	0.2
Drell-Yan	74.2	1.2
Single top	33.1	1.1
ZH	88.8	10.7
Dibosons	90.0	5.0

sample	Efficiency at 300 GeV, [%]	Efficiency at 900 GeV, [%]
signal (bbZZ)	58.1	91.1
signal (bbWW)	25.9	96.3
$t\bar{t}$	13.6	0.2
Drell-Yan	39.0	0.8
Single top	13.0	0.2
ZH	56.0	8.4
Dibosons	51.4	6.2

5.3 Signal and background characteristics

The signal region is further purified removing backgrounds by applying the cut on the BDT output (Table 5.2 contains the efficiency numbers for the BDT cut). The first set of BDT variables in the early version of the analysis included 30-50 variables, which could potentially discriminate signal from the background. The set contained variables related to the kinematic properties of the signature, as well as a dozen of angular variables. After the first optimization of the BDT training and produced ranking of variables, nine best variables were determined and chosen to be used for the final analysis. Removal or addition of other variables did not improve the performance significantly. To simplify the analysis, the same set of nine variables is used in both low and high mass trainings and for both spin hypotheses.

With 16 masses points in the range from 250 to 1000 GeV, one can: train 16 discriminants, train one complex hyperparametrised neural network, split the mass range into regions with the similar kinematics and thus train only few BDTs. The latter is the approach that has been adopted by mature (legacy) HH analyses, and we are following the same procedure. We split the mass range into two: low mass and high mass (à la HIG-17-002 and HIG-17-008). These simplification costs some performance loss but allows analysis to proceed with just two BDTs instead of training one BDT per mass point, which would require more than a dozen of trainings per heavy resonance. In case of the infinite statistics, training a dedicated BDT for each signal mass hypothesis would give a better performance, but in our case we are statistics dominated, thus training only two BDTs also has benefits in terms of the size of the signal sample, absence of the overtraining etc. In addition, the adopted path saves computational resources. Lastly, physics-wise, bbZZ signature is not the most sensitive, bb$\gamma\gamma$ is due to an excellent CMS diphoton mass resolution. Thus, the difference in sensitivity is a factor of 30-100 depending on the mass. Therefore, training a dozen of BDTs is clearly impractical. For more discussion on the topic please refer to the chapter 6.

The low/high mass boundary value for HH analyses is chosen typically in the range 300-450 GeV. In our case the performance of the boundary around 300 GeV (area under the ROC curve for low mass BDT is 0.9138 and 0.9805 for high mass BDT) is similar to the boundary option at the 450 GeV (area under the ROC curve for low mass BDT is 0.9086 and 0.9957 for high mass BDT), and to the one in the middle of the range (area under the ROC curve for 400 GeV for low mass BDT is 0.9074 and 0.9928 for high mass BDT). Therefore, we chose the value of 450 GeV, which is also a choice of the bbbb analysis [57]. Upon running the full analysis chain up to the expected limits, the choice of 450 GeV was verified to be the best split point option: the usage of the high mass BDT at the 400 GeV or low mass BDT at the 500

Table 5.3: Number of events surviving analysis cuts corresponding to the last entry in the 5.3 .

Process, mass point	ee channel, %	mm channel, %
bbZZ, 300 GeV	2256	4511
bbWW, 300 GeV	53	85
bbZZ, 900 GeV	8034	12963
bbWW, 900 GeV	12	23

GeV was yielding suboptimal results thus confirming the mass boundary choice.

Splitting the mass range into two regions, we arrive at the low mass BDT, which merges (with the weight '1') seven signal samples: 250, 260, 270, 300, 350 400, 450 GeV, and the high mass BDT, which combines nine signal samples of masses: 500, 550, 600, 650, 700, 750, 800, 900, 1000. In each case the composition of the background is the same, it is a mix (by cross section) of $t\bar{t}$ and Drell-Yan plus jets.

Cut flow for ee and $\mu\mu$ channels from the generator level up to before the BDT selection is shown on the figures 5.3. In the cut flow table 5.3 the following definitions are used: very loose selection means all GsfElectrons and Muons from the basic collections that match generator level electrons/muons and pass the very minimal kinematic cuts; loose selection means loose POG selection consisting of kinematic cuts, impact parameters dxy and dz, and iso cuts. Shown final efficiency values are given in terms of the number of events 5.3:

5.4 Data and MC comparison

BDT selection is applied in the signal region only, we are not cutting on BDT for control regions, therefore, all the mass points belonging to the low mass region (and separately to the high mass region) have the same background and data distributions. Thus, we provide plots for two mass points: one mass point representing low mass

	2 very loose muons	2 loose muons	mva ID	leading pt and eta gap	iso<0.15	trigger	>=2b-jets, Hbb and Zll cuts
bbWW300	100.0	41.8	21.6	20.3	17.8	16.6	0.2
bbZZ300	100.0	87.4	61.6	56.7	43.0	40.7	10.4
bbWW900	100.0	53.5	15.8	14.6	10.5	9.9	0.1
bbZZ900	100.0	84.0	63.3	59.7	53.6	50.2	15.1

	2 very loose electrons	2 loose electrons	mva ID	leading pt and eta gap	iso<0.06	trigger	>=2b-jets, Hbb and Zll cuts
bbWW300	100.0	38.8	18.9	17.4	13.0	10.0	0.1
bbZZ300	100.0	68.2	46.3	43.9	24.7	23.1	5.9
bbWW900	100.0	38.5	14.9	13.1	5.5	4.8	0.0
bbZZ900	100.0	71.4	46.0	43.7	36.0	33.9	10.0

Figure 5.3: Cut flow for mm (top) and ee (bottom) channels.

region, 300 GeV, and one mass point representing high mass region, 900 GeV. Signal bbZZ and bbWW rates for all plots are multiplied additionally by a factor of 500 purely for the visualization purpose and do not go in the real analysis.

Postfit plots that include SR in the simultaneous fit with control regions, hence a common jargon name "Full postfit" plots, in contrast to the control regions only type of the fit, or a control regions plus signal region sideband. Figures 5.4 - 5.5 show data and MC comparison in the SR, CRDY, and CRTT. For both ee and $\mu\mu$ channels, low and high mass regions. The latest style plots produced for the analysis public document (Physics Analysis Summary called "PAS") can be found at Fig. 5.4 for the graviton case and Fig. 5.5 for the radion case.

Distributions of nine variables that go into the BDT have been studied in depth during the pre-approval process and are available in the Appendix of the analysis note [58]. All variables show good data/MC agreement after applying postfit scale factors (not to be confused with the POG recommended scale factors in the section below). The most important variables in this analysis, namely the BDT itself and the variable that we fit, $\tilde{M}_T$(HH), are shown in the Fig. 5.4 for graviton and in Fig. 5.5 for the radion.

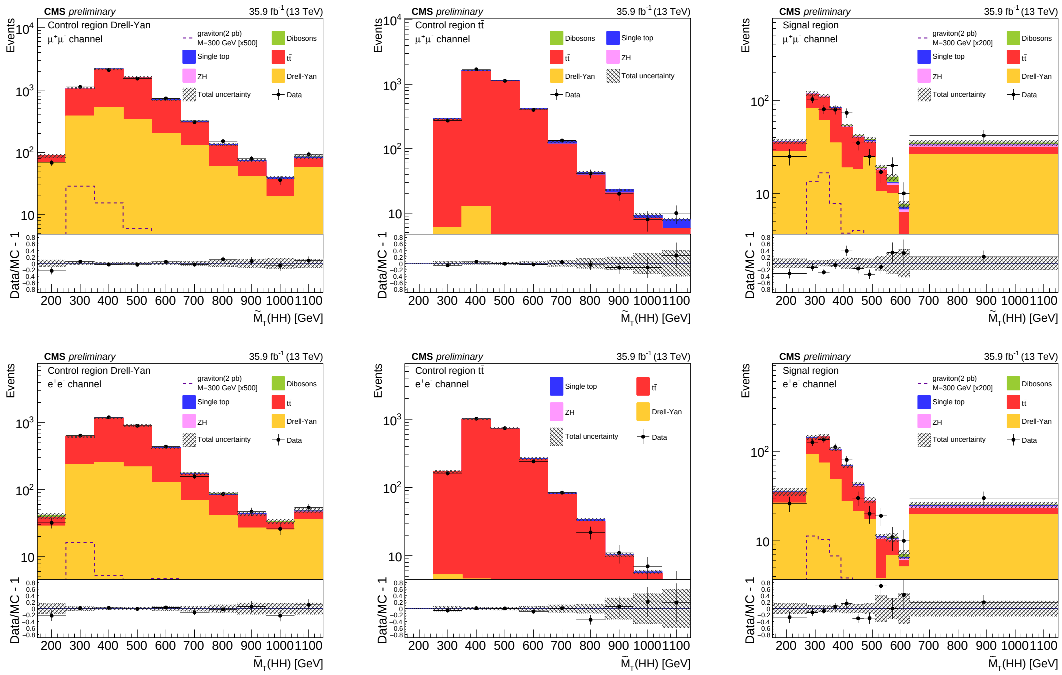

Figure 5.4: Transverse mass of the reconstructed HH candidates for data, the simulated signal graviton sample for the 300 GeV mass hypothesis, and simulated backgrounds scaled according to the fit results. The top row shows the figures for the muon channel while the bottom row is for the electron channel. For each row, the left plot is for the Drell-Yan control region, the middle is for the $t\bar{t}$ control region, and the right is for the signal region. Signal normalization choice is discussed in the text. The crosshatched area represents the sum of statistical and systematic uncertainties.

5.5 Scale Factors

Electron ID and ISO scale factors, as well as HLT scale factors (Fig. 2.1), have been computed by VHbb group, which ntuples and analysis setup we reutilise. Scale factors have been presented at the EGamma physics object groups (POG) meeting [59] and fully approved. We reuse those scale factors and apply them to our MC samples.

Muon ID scale factors, as well as ISO scale factors, have been derived separately for runs G/H and B/C/D/E/F runs (2016 data at LHC has been split into several "runs") and then luminosity averaged to obtain the final numbers [60]. Tracker scale factors (2.1) are taken from the Muon POG twiki page [61] and used as is. HLT dimuon scale

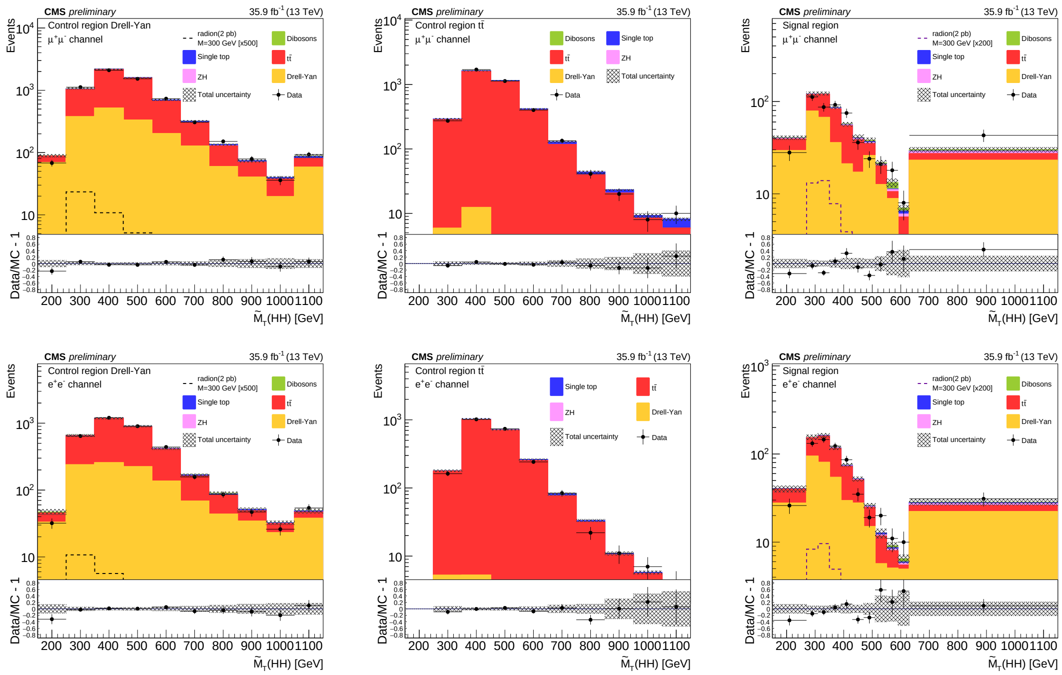

Figure 5.5: Transverse mass of the reconstructed HH candidates for data, the simulated signal radion sample for the 300 GeV mass hypothesis, and simulated backgrounds scaled according to the fit results. The top row shows the figures for the muon channel while the bottom row is for the electron channel. For each row, the left plot is for the Drell-Yan control region, the middle is for the $t\bar{t}$ control region, and the right is for the signal region. Signal normalization choice is discussed in the text. The crosshatched area represents the sum of statistical and systematic uncertainties.

factors were derived by VHbb group and further approved by the muon POG. These scale factors were derived separately for run H (Fig. 2.3) and B/C/D/E/F/G (Fig. 2.2) runs and then luminosity averaged [62]. On top, separate scale factors are calculated for the dZ requirement of HLT_Mu17_TrkIsoVVL_Mu8_TrkIsoVVL_DZ_v* OR HLT_Mu17_TrkIsoVVL_TkMu8_TrkIsoVVL_DZ_v* triggers, using dilepton events that have already passed the HLT_Mu17_TrkIsoVVL_Mu8_TrkIsoVVL_v* OR HLT_Mu17_TrkIsoVVL_TkMu8_TrkIsoVVL_v* triggers (Fig. 2.4).

Chapter 6

BDT Discriminant

The Toolkit for Multivariate Data Analysis with ROOT (TMVA) package is used to perform BDT training [63]. This ROOT-integrated library enables the usage of the machine learning techniques for the physics data analysis and is commonly used.

6.1 Construction of the BDT

In this analysis we use the set of nine variables to construct the BDT. These variables are the same in both low and high mass trainings and for both heavy resonances.

Some variables are important only in the specific mass regime, some are ranked highly universally across the whole mass range. For example, in the low mass regime $E_{\mathrm{T}}^{\mathrm{miss}}$ and H $\rightarrow b\bar{b}$ mass are powerful discriminators against Drell-Yan to leptons plus jets. That is why these observables are located in the top three variables of the ranking for low mass BDT (Figs. 6.1). In the high mass regime the leverage is in the boost, therefore, $\Delta R = \sqrt{\Delta\phi^2 + \Delta\eta^2}$ variables, as well as p_T-related variables show high performance (Figs. 6.1). Namely, p_T of both Higgs bosons, Z boson, and also separation ΔR between two b-jets and also ΔR between two leptons. It is worth noting that H $\rightarrow b\bar{b}$ mass is a powerful discriminator ranked highly for all mass regimes and both channels. Plots of input variables and correlations are shown on

	Rank	Importance, %
1	dR_bjets	13.9
2	met	12.1
3	Hbb mass	11.9
4	pT(ZZ)	11
5	dR_leps	10.9
6	Hbb pT	10.7
7	Z pT	10.2
8	M(ZZ)	10.1
9	Z mass	9.26

	Rank	Importance, %
1	dR_leps	14.1
2	Hbb mass	13.7
3	dR_bjets	13.2
4	Hbb pT	12.1
5	Z pT	11.5
6	pT(ZZ)	11.3
7	met	10.3
8	M(ZZ)	7.7
9	Z mass	6.1

	Rank	Importance
1	dR_bjets	13.0
2	met	12.2
3	Hbb mass	11.9
4	Hbb pT	11.3
5	Z pT	11.1
6	pT(ZZ)	10.9
7	dR_leps	10.5
8	M(ZZ)	9.7
9	Z mass	9.5

	Rank	Importance
1	Hbb mass	13.8
2	dR_bjets	13.1
3	dR_leps	12.9
4	Hbb pT	11.7
5	pT(ZZ)	11.3
6	Z pT	11.1
7	met	11.0
8	M(ZZ)	8.8
9	Z mass	6.2

Figure 6.1: Ranking of variables in the BDT training for electron(muon) channel at the top(bottom). Left: low mass BDT. Right: high mass BDT.

the Figs. 6.3, 6.9, 6.7, 6.8, 6.13, 6.14.

It is hard to get high performance in the low mass training, since this is where all the backgrounds are concentrated (Figs. 6.3, 6.9). The rate of background in this region is enormous and most variables have similar distributions for signal

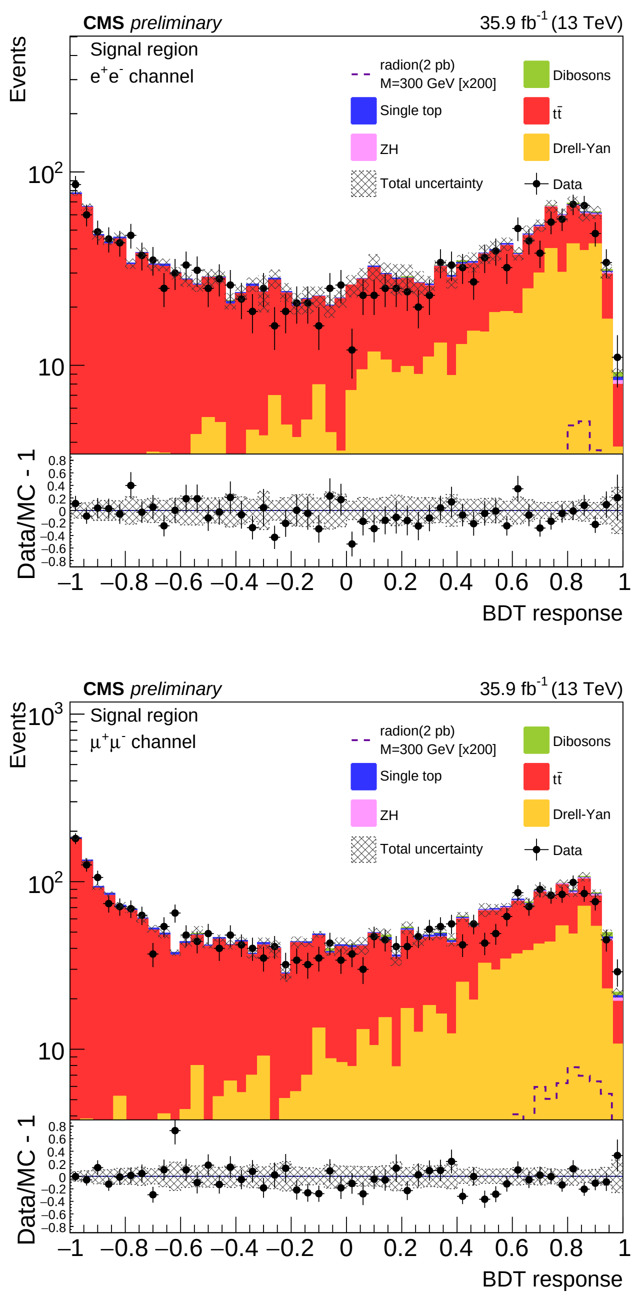

Figure 6.2: BDT plots for radion case, electron(muon) channel at the top(bottom). Signal region, 300 GeV mass hypothesis. For electrons cut is at 0.4, for muons at 0.7. More details at the table 9.1.

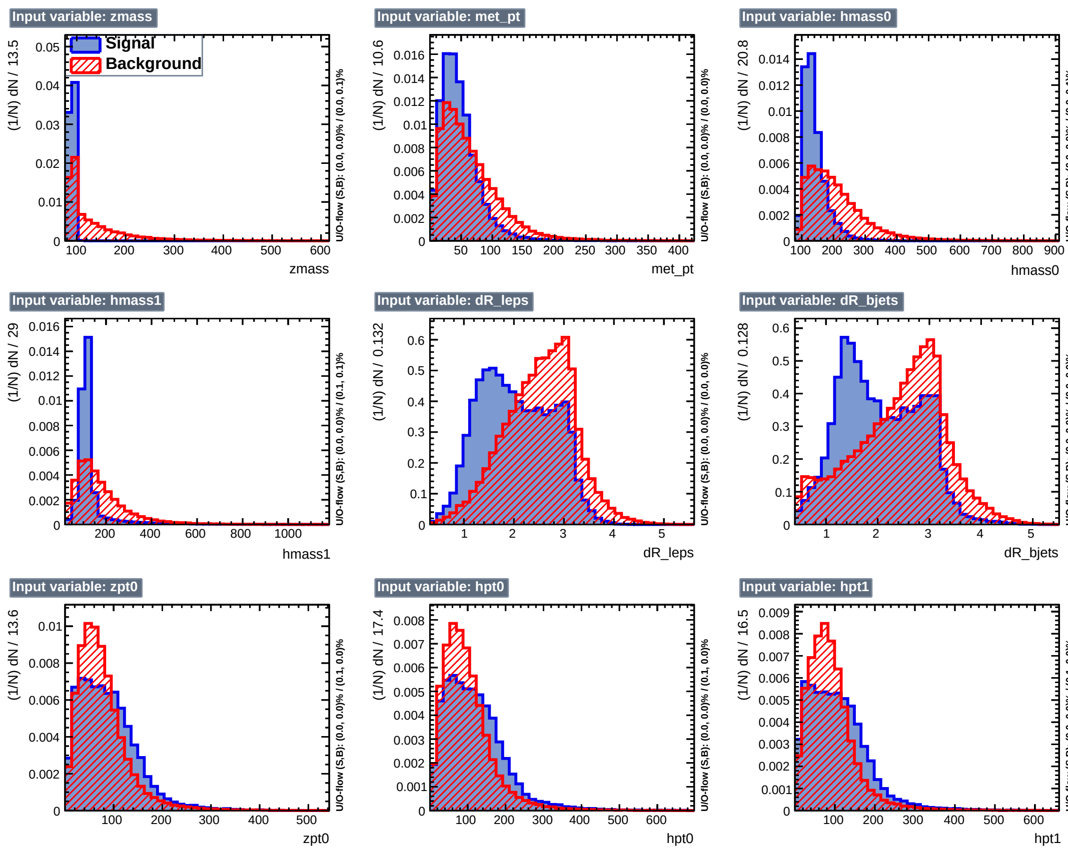

Figure 6.3: Variables used in the low mass training for electron channel. Index ’1’ refers to $b\bar{b}$ and index ’0’ refers to ZZ.

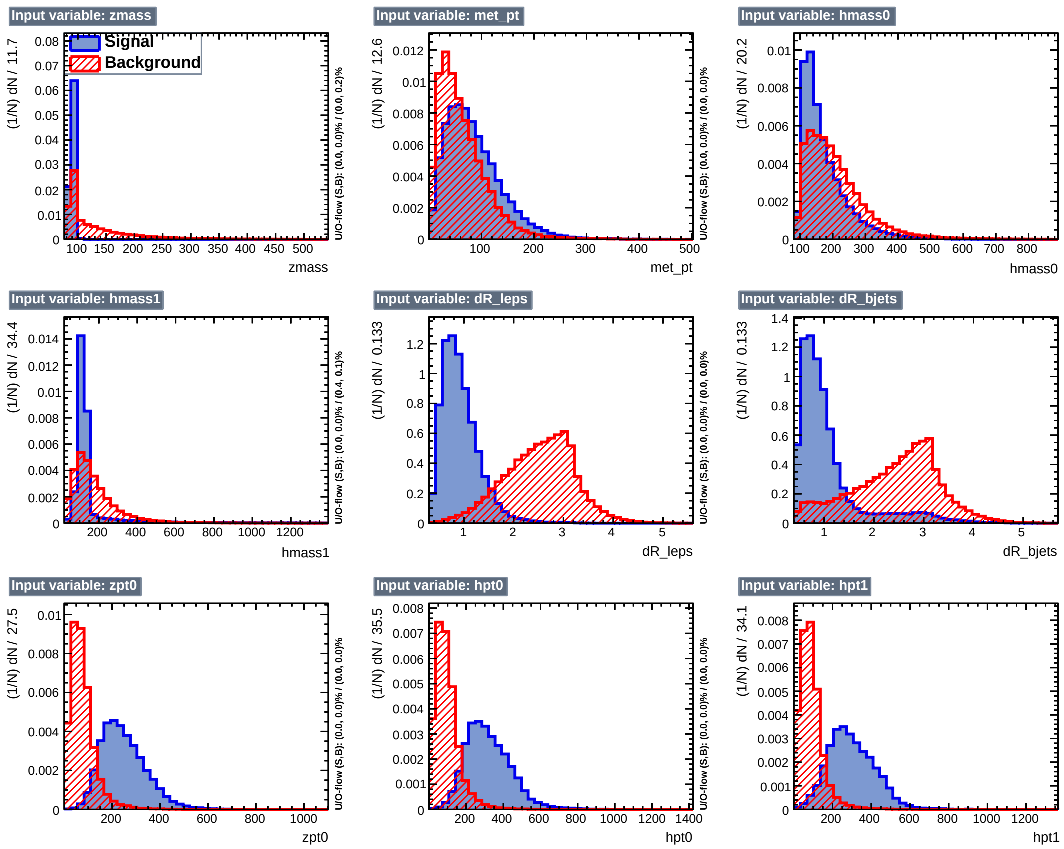

Figure 6.4: Variables used in the high mass training for electron channel.

and backgrounds. However, BDT performance is noticeably better than what can be achieved using a simple linear discriminant method (Figs. 6.5, 6.6, 6.11, 6.12).

Earlier versions of the analysis tried more granular approach to the number of BDTs, up to four BDTs to cover the whole range from 250 to 1000 GeV. But it was shown that this added extra complexity brings almost no improvement, while in fact is error prone and computationally twice more expensive. This is why other HH analyses also split the whole mass range only in two subranges and we followed the same suggestion. The BTD plots for radion case in the signal regions for 300 GeV mass hypothesis are shown at Fig. 6.2.

Performance of the high mass training is perfect (Figs. 6.4, 6.10,). The ROC curves are close to the top right corner of the efficiencies space, which means a high signal efficiency is achieved along side with the low efficiency of the background. This is due to the fact that most backgrounds peak in the low mass region. Even linear discriminant is performing well in this situation (Figs. 6.5, 6.6, 6.11, 6.12).

For completeness purpose and research reproducibility, it is worth mentioning in this paragraph the technical details. The following TMVA specific parameters have been used for the BDT training (most parameters are default ones since no significant improvement was observed when varying the parameters one at a time): NTrees = 800, BoostType=Grad, Shrinkage=0.1, UseBaggedBoost=True, GradBaggingFraction=0.5, SeparationType= GiniIndex, nCuts=30, and MaxDepth=3.

Electrons and muons have been optimised separately but BDT trainings show similar performance (Fig. 6.6 and 6.12). BDT distributions for data and MC comparison are created with the nominal values for the lepton and b jet scale factors. When shape systematics is considered to produce final limits, BDT shapes are varied using 'Up' or 'Down' versions of the scale factors and all the input variables to the BDT are modified in the similar fashion as well. The BDT plots shown below are

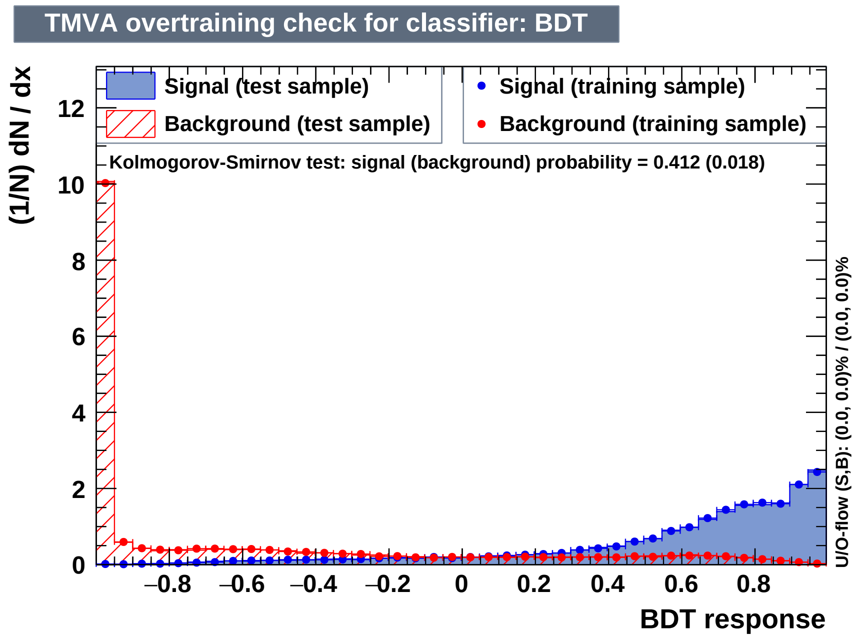

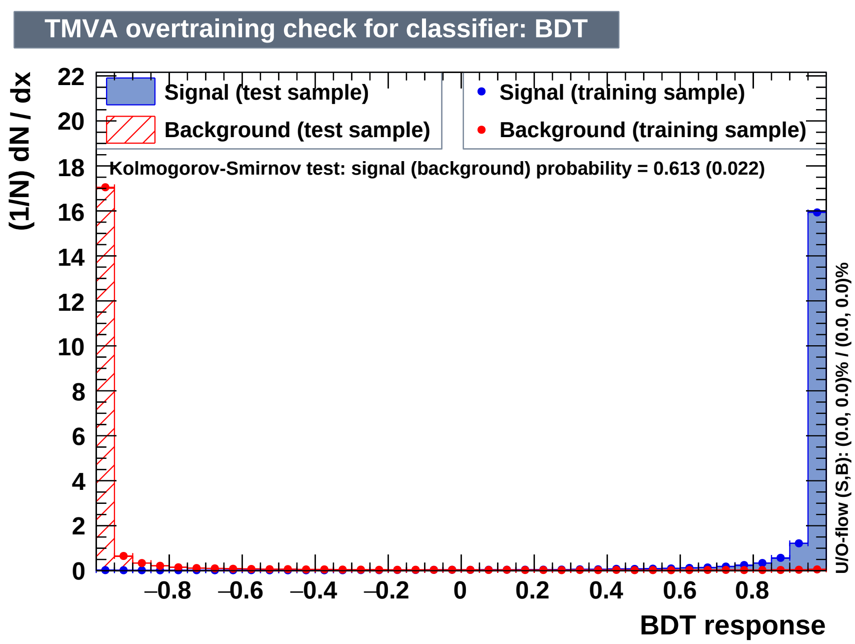

Figure 6.5: BDT discriminants for electron channel. Top: low mass training. Bottom: high mass training.

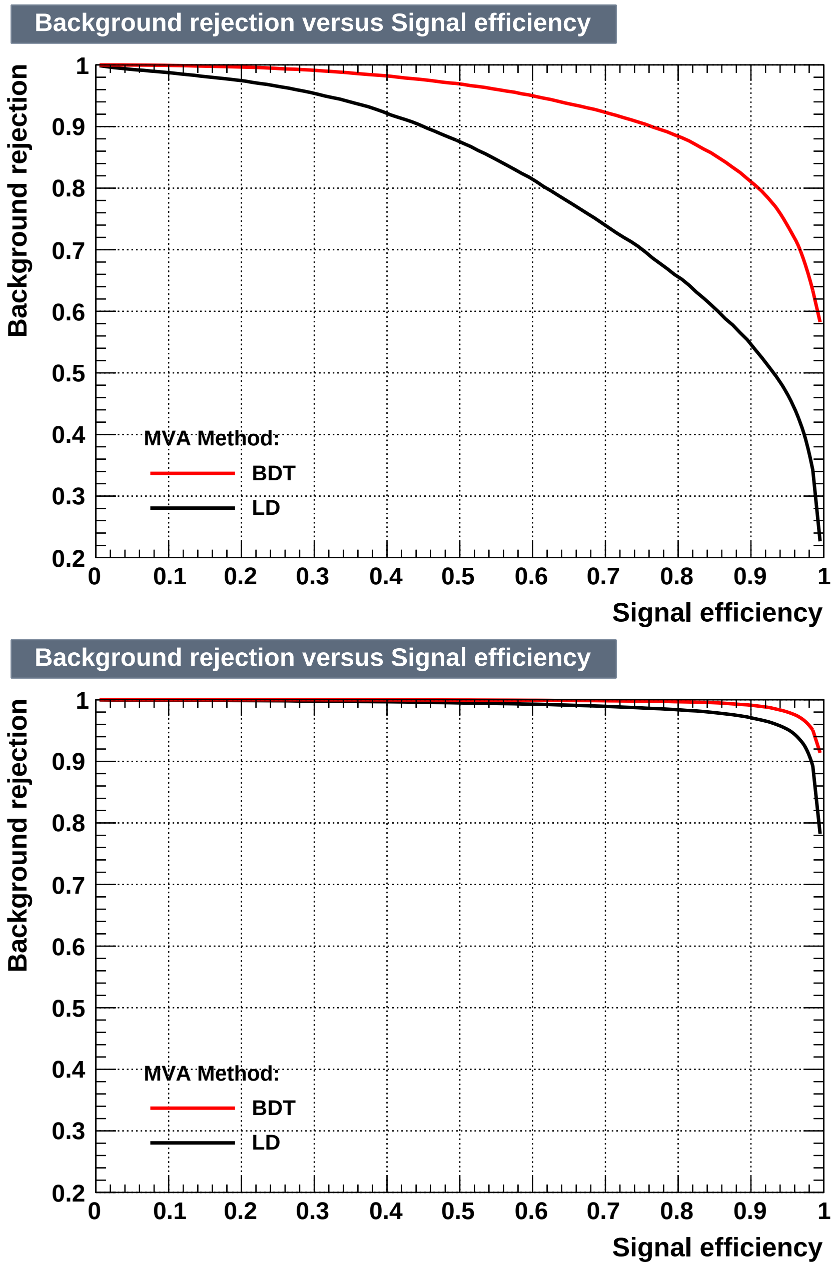

Figure 6.6: ROC curves for electron channel. Top: low mass training. Bottom: high mass training.

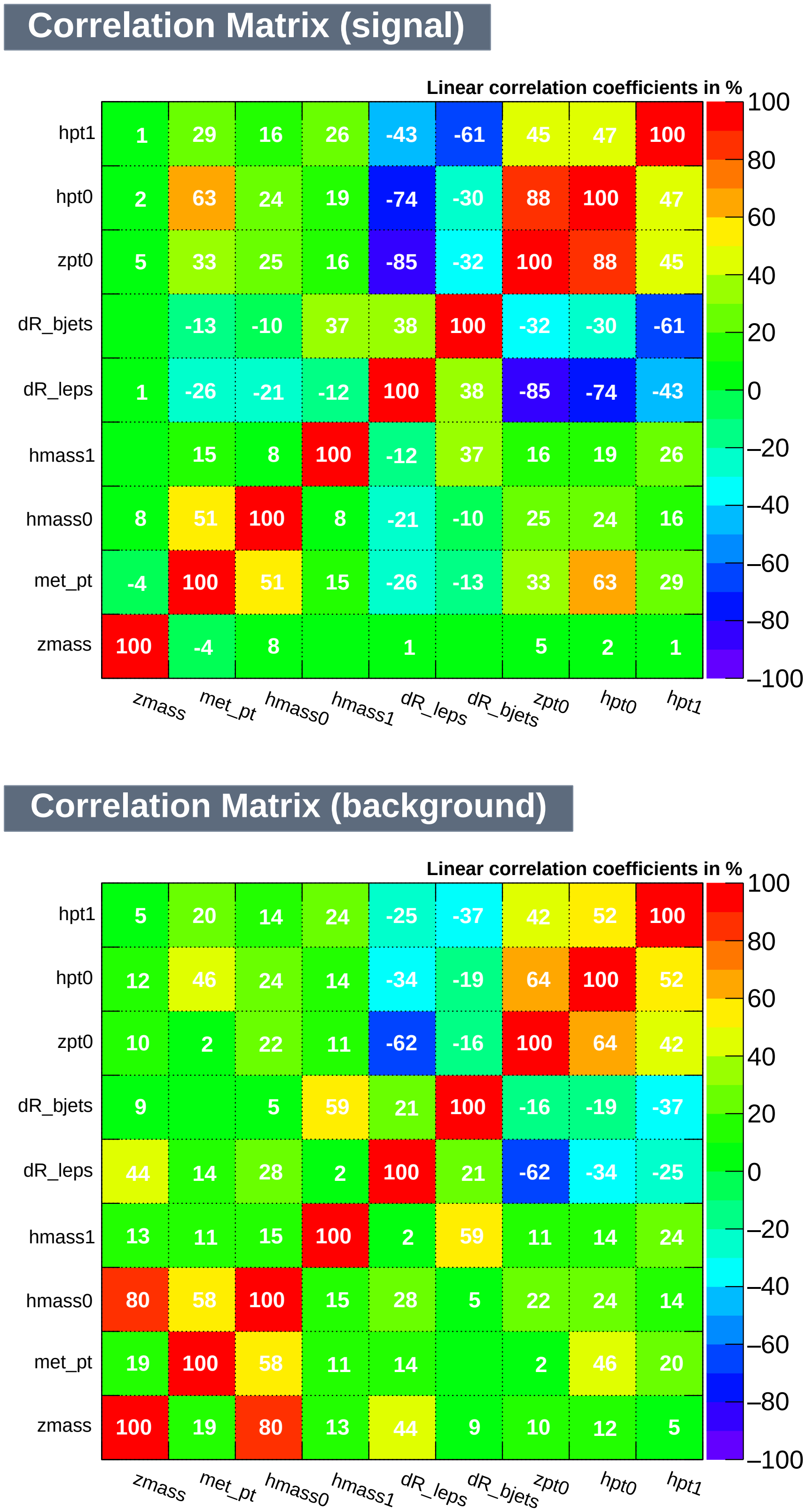

Figure 6.7: Input variables correlations for electron channel, low mass training. Top: signal sample mix. Bottom: background sample mix.

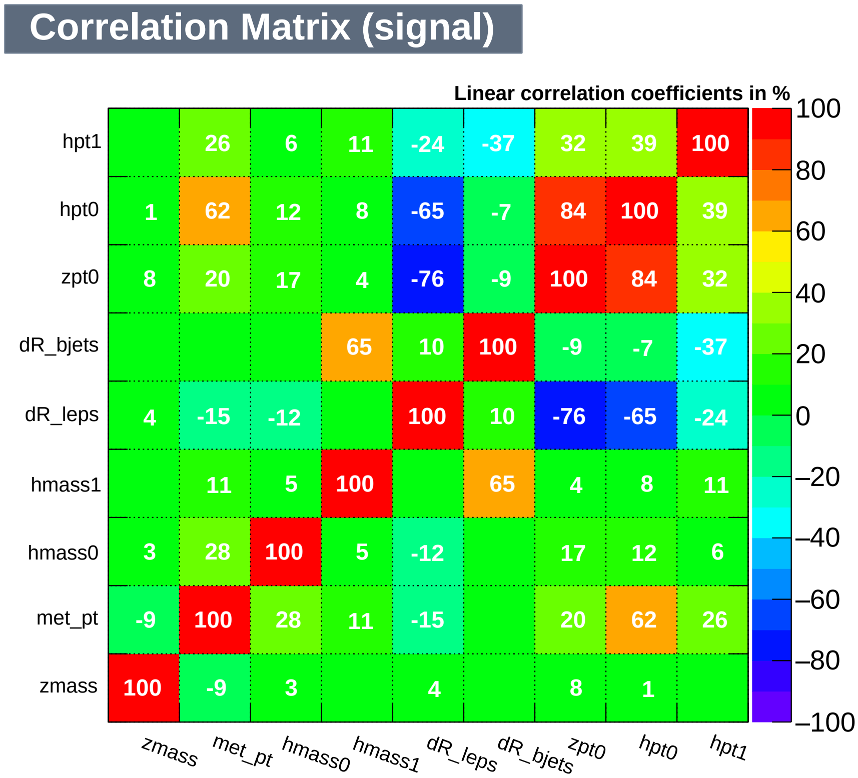

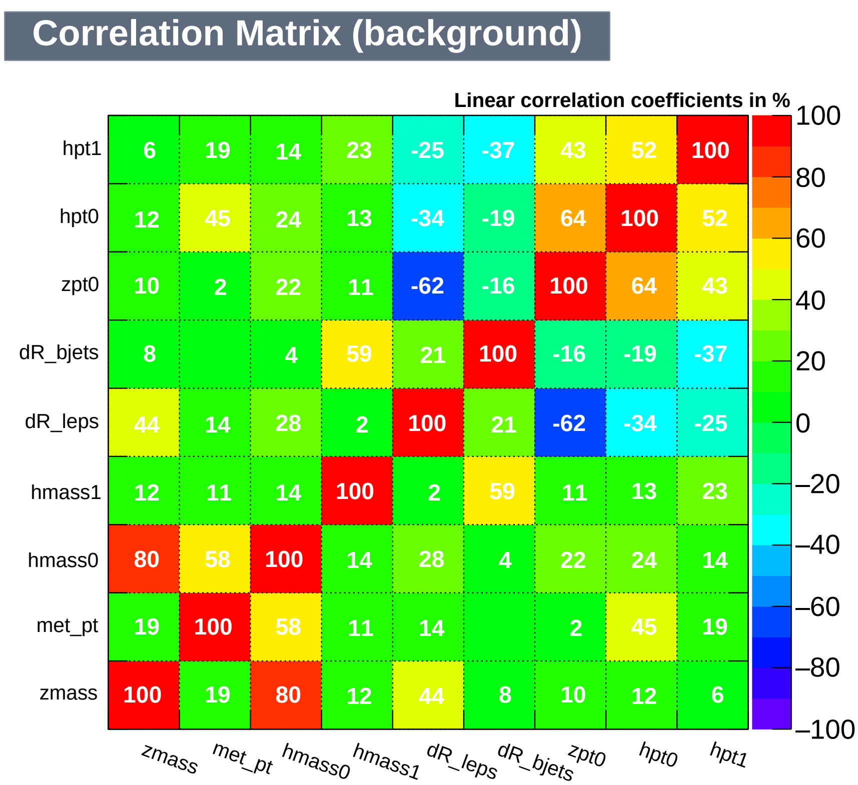

Figure 6.8: Input variables correlations for electron channel, high mass training. Top: signal sample mix. Bottom: background sample mix.

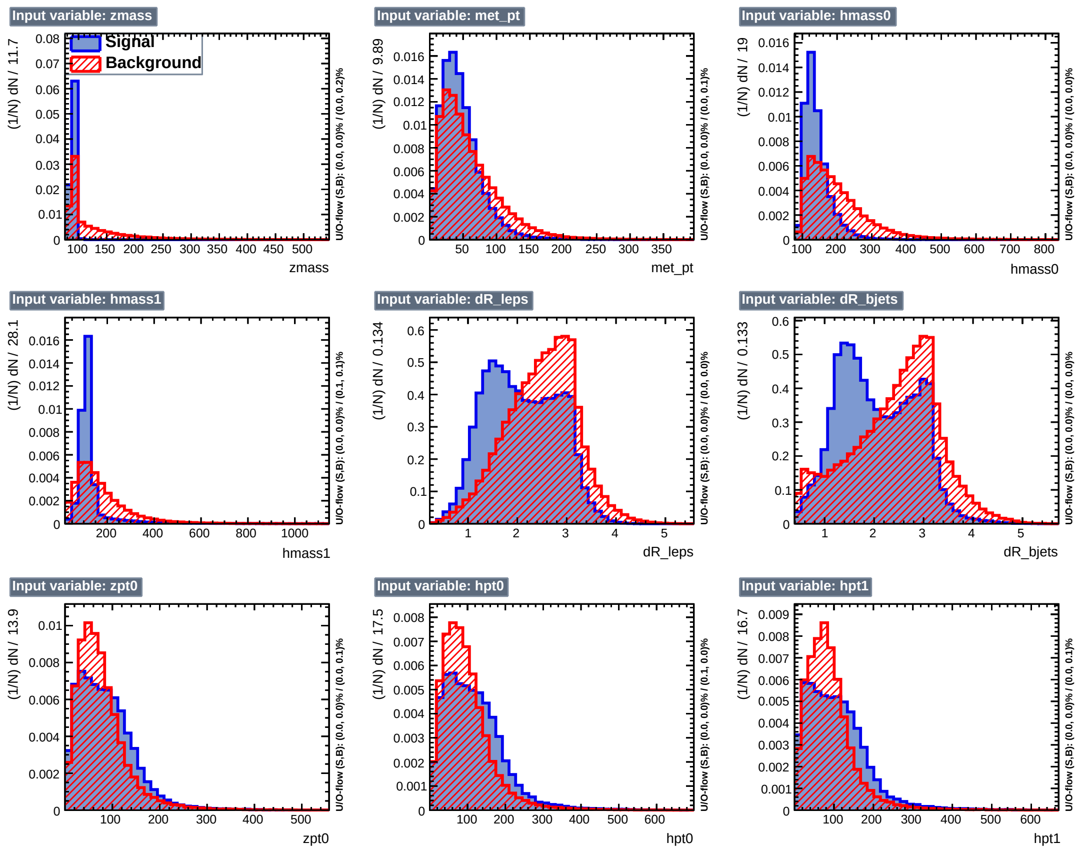

Figure 6.9: Variables used in the low mass training for muon channel. Index '1' refers to $b\bar{b}$ and index '0' refers to ZZ.

further modified applying postfit values of DY and $t\bar{t}$ normalizations returned from the Maximum Likelihood fit performed with the real data.

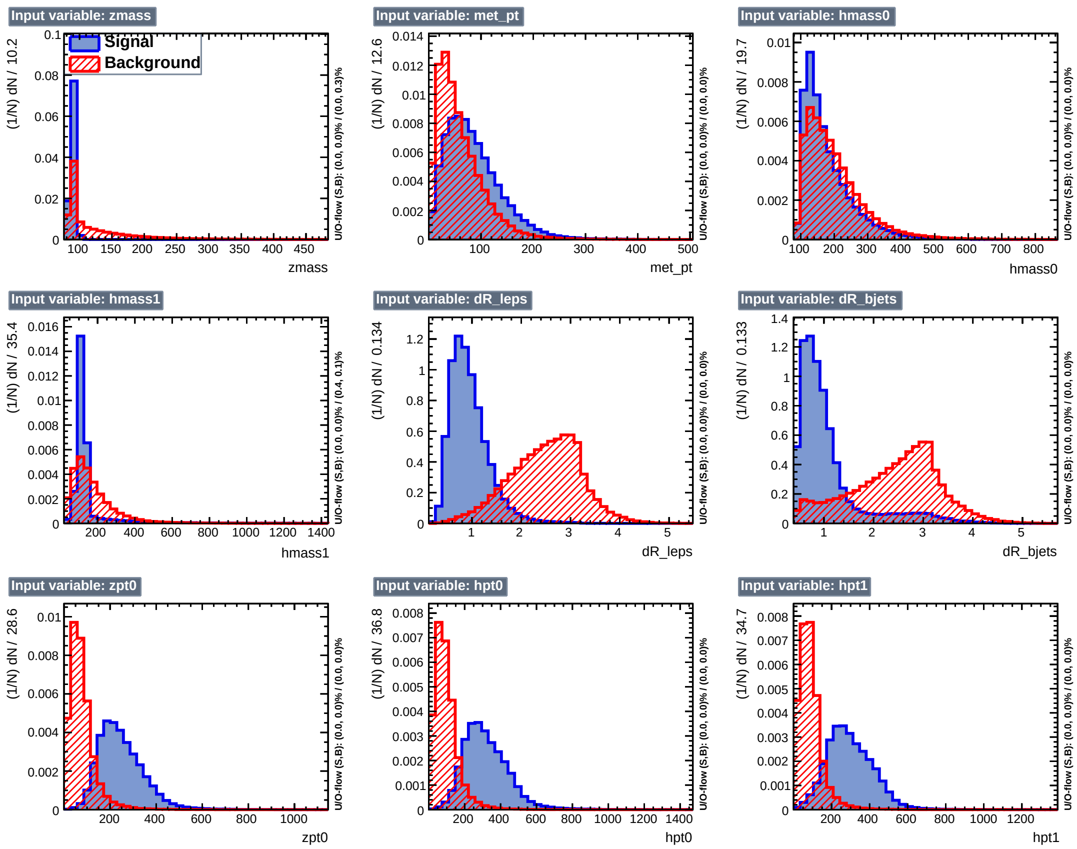

Figure 6.10: Variables used in the high mass training for muon channel.

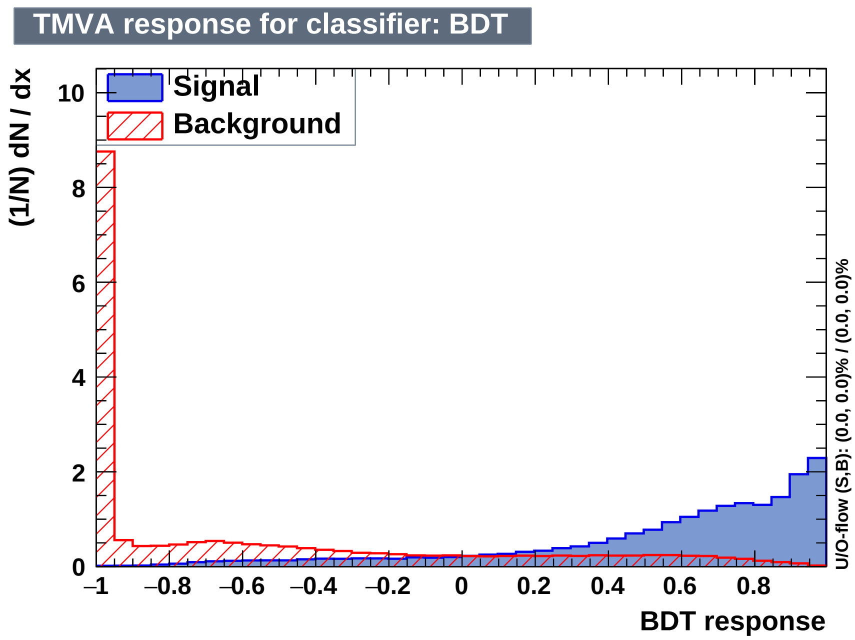

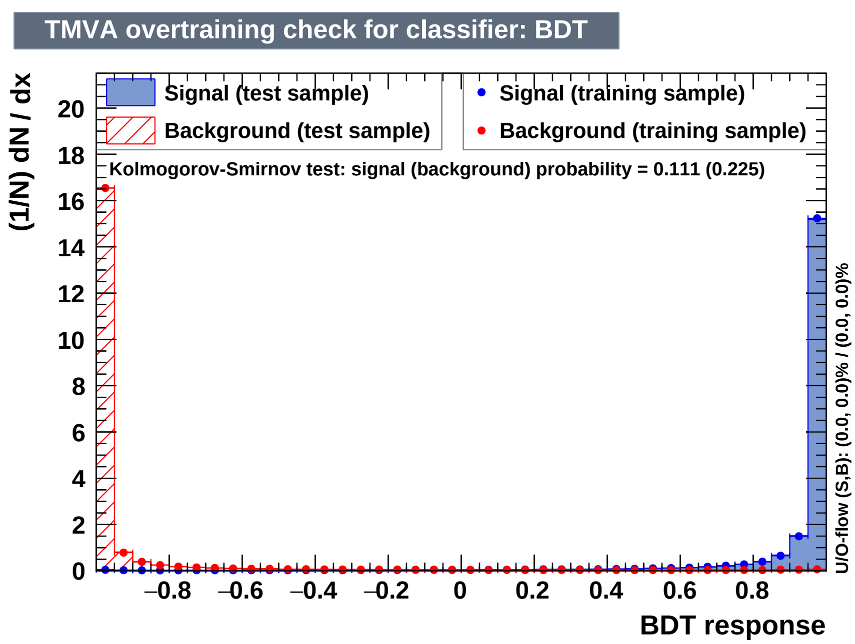

Figure 6.11: BDT discriminants for muon channel. Top: low mass training. Bottom: high mass training.

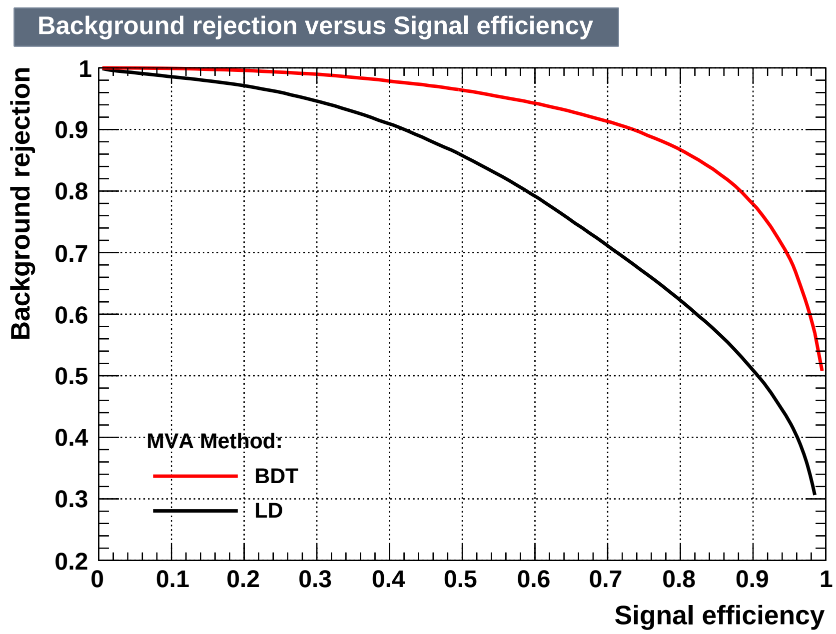

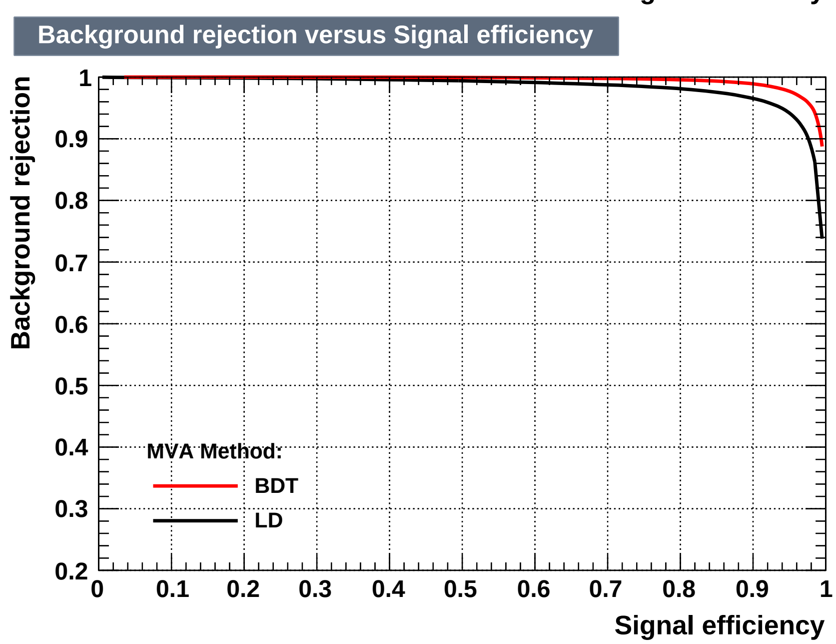

Figure 6.12: ROC curves for muon channel. Top: low mass training. Bottom: high mass training.

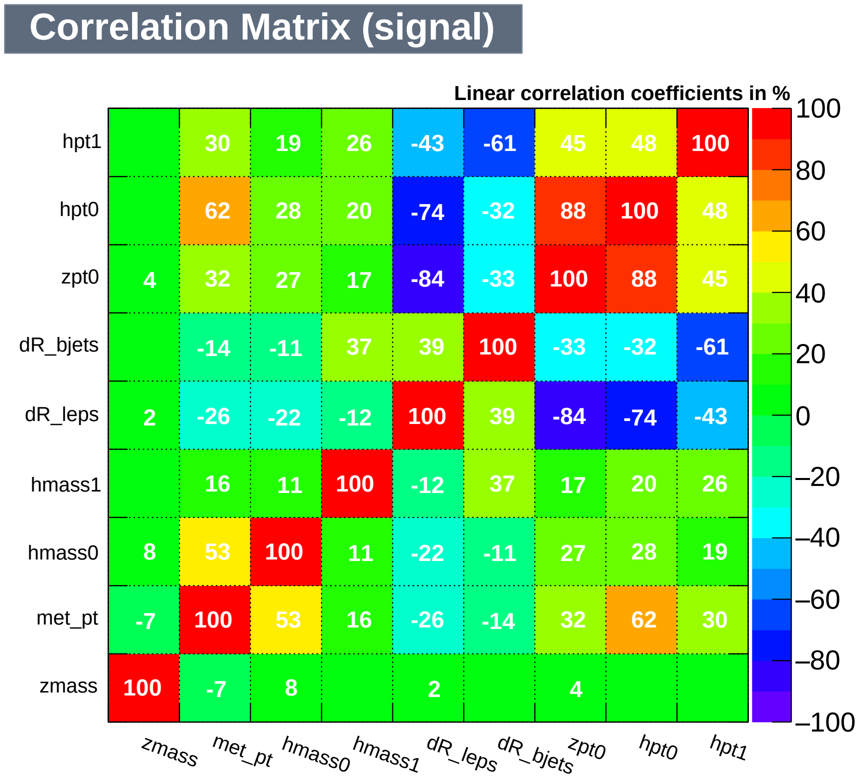

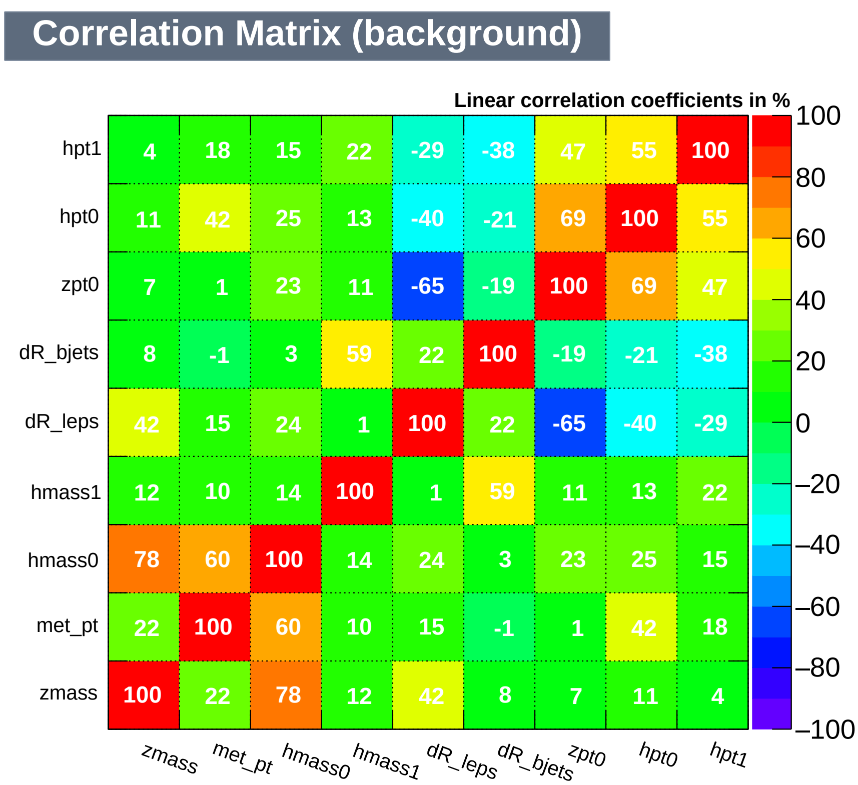

Figure 6.13: Input variables correlations for muon channel, low mass training. Top: signal sample mix. Bottom: background sample mix.

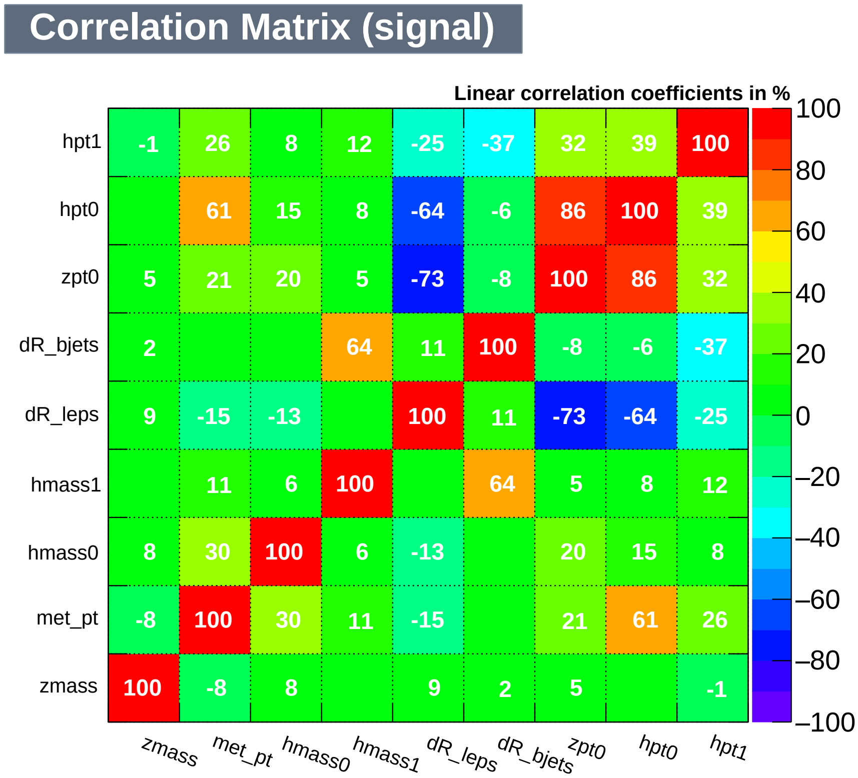

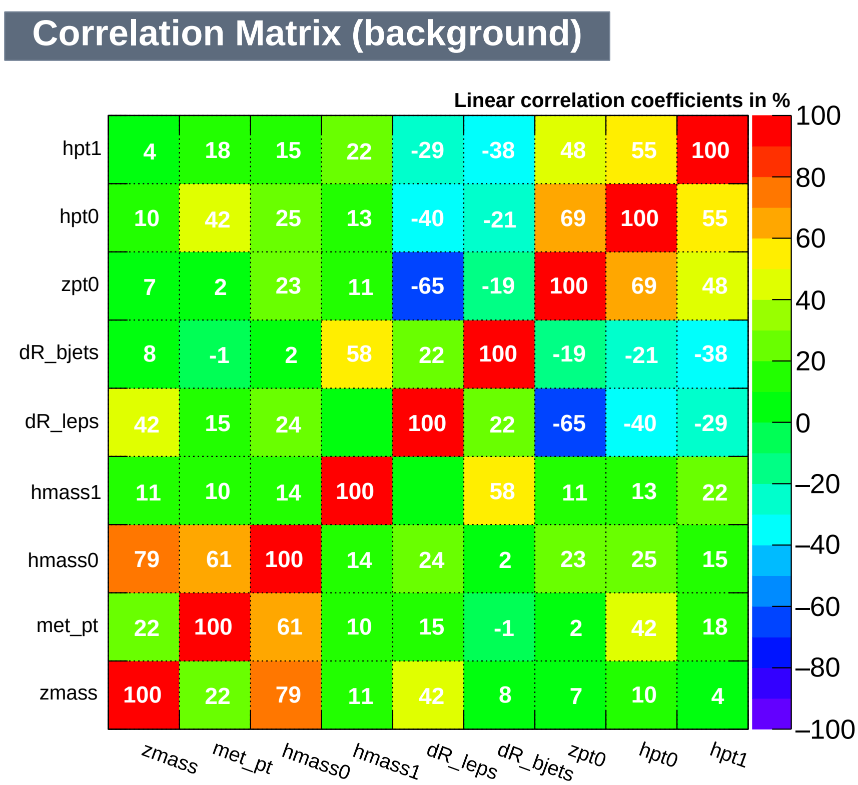

Figure 6.14: Input variables correlations for muon channel, high mass training. Top: signal sample mix. Bottom: background sample mix.

Chapter 7

Systematic Uncertainties

Systematic uncertainties that affect the sensitivity of our di-Higgs search come from a variety of sources such as theoretical uncertainties on cross sections or proton structure, experimental uncertainties related to the modelling of the detector response, the amount of collected data, and the discrepancies between the simulated samples and the real data.

Systematic uncertainties can be divided into two broad categories: those affecting only the yields of selected events from different processes (the "normalization" uncertainties) and those that, in addition to the change in rate, may distort the shape of the $\tilde{M}_T(\mathrm{HH})$ distribution used in the extraction of the limits (the "shape" uncertainties).

7.1 Normalization uncertainties

The sources of systematic uncertainties that affect normalizations are discussed in the list below. The sizes of some systematic uncertainties may vary depending on the resonance mass hypothesis and the decay channel of the leptonically decaying Zboson, in which cases ranges of the uncertainty values are listed. Normalization uncertainties discussed in this section do not affect the normalizations of the $t\bar{t}$ and DY backgrounds because those are determined from data during the simultaneous fit of the signal and control regions.

- **Luminosity** - CMS estimated this uncertainty on the integrated luminosity of the CMS 2016 data set to be 2.5% [?]. This uncertainty directly affects the expected event yields for the signal processes as well as all background processes except for the two dominant backgrounds, DY and $t\bar{t}$.

- **Pileup** - Signal and background event yields depend on the accuracy of the reproduction of pileup interactions in each simulated event. The effect of pileup is considered on each process. The recommended nominal value of 69.2 mb is used for the total inelastic pp cross section, for Down and Up variations, the values of 66.02 and 72.38 mb are used respectively, reflecting the imperfect knowledge of the total inelastic proton-proton interaction cross section at 13 TeV. The effect is seen only in the normalization and we, thus, consider this a normalization uncertainty and assign the value of 6%.

- **Proton PDF** - The systematic bias associated with the limited knowledge of the interacting proton content is evaluated using an ensemble of a hundred of PDF replicas from the NNPDF set [?] following the PDF4LHC prescription [?,?] and the RMS of the resulting process normalizations is taken as a measure of the bias. It is found to be of order 5%.

- **QCD scales** - Theoretical uncertainties in the QCD factorization and renormalization scales affect the expected yield of the signal and background events, excluding the $t\bar{t}$ and DY yields as mentioned earlier. This uncertainty is estimated by varying independently these two scales in simulation by factors 0.5 and 2 with respect to the nominal values of the scales. The unphysical cases with one of the scales fluctuating up while the other fluctuates down are discarded. In each bin of the HH transverse mass distribution the maximum and minimum variation are used to build an envelope around the nominal shape, resulting in the effect of the size 4-6% on the processes' yields.

- **Missing transverse energy/momentum** - Clustered energy in jets and leptons undergo energy corrections during event reconstruction, however, neutral hadrons and photons that do not belong to any jet ("unclustered energy") and jets with low transverse momenta (below 10 GeV) lack such corrections. This results in a small systematic bias in the reconstructed missing transverse momentum. $\not{E}_{\mathrm{T}}$ enters the $\tilde{M}_T$(HH) variable, thus the effect of the unclustered energy has to be studied. We shift the energy of each particle not contained in jets or contained in low-p_{T}jets by its uncertainty Up and Down. Such variations affect the event yields of signal and background processes at about 3% level but do not have a visible effect on the shape of the HH transverse mass, thus this source is categorised as a "normalization" systematic source.

7.2 Shape uncertainties

Several sources of systematic uncertainties affect not only the rate but also the shapes of various kinematic distributions which are inputs to the BDT or a part of the $\tilde{M}_T$(HH) construction, the BDT discriminant itself, and the shape of the $\tilde{M}_T$(HH) distribution. Each source is varied separately within one standard deviation up and down, and the effect is propagated through all related variables resulting in the nominal shape of the HH invariant mass distribution and two modified shapes corresponding to the Up and Down variations. Such triplet of shapes is prepared for each channel, each mass hypothesis, and for all processes.

All these shapes are fit simultaneously in the signal extraction likelihood fit. The discussion of the these sources of uncertainties follows.

- **Lepton efficiency** - The effect of the detector on the reconstruction of the lepton: identification and isolation selection criteria, and the requirement to pass trigger selection requirements are studied separately and are used to account for data/MC discrepancies. The corrections are derived from large dedicated samples of Zboson decays and also have an error associated with the procedure. The uncertainty on lepton efficiency corrections are derived as a function of lepton p_T and η and is propagated to the final $\tilde{M}_T$(HH) distributions. The effect of these uncertainties is sub-percent for the muon channel and up to 6% for the electron channel.

- **Jet energy scale** - The uncertainty on the jet energy scale affects H $\rightarrow b\bar{b}$mass and p_{T}, which are inputs to the BDT. In addition, jet energy scale directly affects H $\rightarrow b\bar{b}$mass and $\not\!\!E_{\mathrm{T}}$, which are used during the construction of the HH invariant mass. Jet energy scale is varied Up and Down within one standard deviation of its uncertainty as a function of jet p_T and η, and the effect on the jet kinematics and on the $\not\!\!E_{\mathrm{T}}$ is calculated and propagated through the steps of the measurement yielding the variation of the HH invariant mass shape. Jet energy scale uncertainty, with all factors combined, has the effect on the yields of the signal and some background components as large as 5 to 10%.

- **Jet energy resolution** - Data and MC a different energy resolution, which also affects the final $\tilde{M}_T$(HH) shapes via its effect on the dijet invariant mass for H $\rightarrow b\bar{b}$and its effect on the $\not\!\!E_{\mathrm{T}}$. Jet energy resolution is varied in simulation by one standard deviation as a function of jet p_T and η and the effect is propagated through the steps of the measurement. Its effect on the $\tilde{M}_T$(HH) yield is typically order of 0.5%.

- **b-tagging and mistagging** - The efficiency to tag a q_b-jet and the probability to misidentify a different flavor or a gluon jet and tag it as a q_b-jet is corrected in MC samples by factors derived from flavor-enhanced jet samples. The uncertainties on these corrections are propagated through the whole analysis setup. The effect of the q_b-tagging efficiency (mistagging/flavor misidentification) is about 5% (7–10%) for the Drell-Yan process and at the sub-percent level for other processes (7–10%).

- **Bin-by-bin uncertainties** - Since the available statistics for the simulated MC samples is limited, the lack of events in some bins of the $\tilde{M}_T$(HH) distribution is addressed by bin-by-bin (BBB) uncertainty. This effect may result in sizeable fluctuations of the bin content of the HH invariant mass shapes that enter the likelihood fit. Therefore, for each bin of the HH invariant mass distributions an individual nuisance parameter is added to the likelihood fit with the Gaussian constraint of one standard deviation of the yield uncertainty in that bin.

Chapter 8

Statistical Analysis

The results in this measurement are obtained with the maximum likelihood fit. We perform a simultaneous fit of the SR and both CRs for both dielectron and dimuon channels using the likelihood function constructed as a product of Poisson terms over all bins of the input $\tilde{M}_T(\mathrm{HH})$ distributions in the three regions (SR, CRDY, CRTT) with Gaussian terms to constrain the nuisance parameters:

$$L(r_{\text{signal}}, r_k|\text{data}) = \prod_{i=1}^{N_{\text{bins}}} \frac{\mu_i^{n_i} \cdot e^{-\mu_i}}{n_i!} \cdot \prod_{j=1}^{N_{\text{nuisances}}} e^{-\frac{1}{2}\theta_j^2}$$

where the product index i refers to the bin of the input distributions, the product index j refers to uncertainties accounted for by the fit model, and n_i is the number of observed data events in the bin i. The mean value for each of the Poisson distributions is computed as:

$$\mu_i = r_{\text{signal}} \cdot S_i + \sum_k r_k \cdot B_{k,i},$$

where k refers to the background process k, and $B_{k,i}$ is the content of the bin i of the background shape for a process k, while S_i is the content of the bin i of the signal shape. The parameter r_k sets the normalization of the background process k while r_{signal} is the signal strength parameter, all r parameters are floating freely in the fit. Two values of the signal strength parameter are of special interest: $r_{signal} = 0$ describes the background-only hypothesis, while $r_{signal} = 1$ corresponds to the case when the HH cross section matches the cross section used for the initial signal normalization inspired by BSM models, 2pb in our case. The terms θ_j represent the set of nuisance parameters that are introduced into the likelihood function as Gaussian constraints.

Figure 5.4(5.5) shows the HH transverse mass distributions for the signal and two control regions for both channels for the graviton (radion) resonance mass hypothesis with normalizations and shapes of all components adjusted according to the best-fit values. The signal sample is normalized to the cross section of 2 pb, a typical value for predictions of WED models (e.g., at 300 GeV), and is further scaled, as indicated on the Figure, to make it clearly visible.

With the given 2016 dataset, the fit results show no evidence for HH production through a narrow resonance, whose width is negligible in comparison to experimental resolution, in the mass range from 250 GeV to 1 TeV. Thus, upper 95 % confidence level limits on the HH production cross section are set using the modified frequentist CL_s approach (asymptotic CL_s) [64–67].

The observed and expected 95% upper CL limits for the full mass range and both resonances are listed in Table 9.2. We produce the standard CMS Brazilian-flag type of plot for the limits, shown in Fig. 9.3. The green and yellow bands correspond to one and two standard deviations around the expected limit respectively. Since 450 GeV is the separation boundary between two mass regions: low mass and high mass, the limit calculation is performed with both of the BDTs at 450 GeV, where the discontinuity is seen in the figure. The Figure also shows the expected production cross section for a RS1 KK graviton/RS1 radion in WED models. This cross section is computed in [2] under the assumption of no mixing with the SM Higgs boson.

Chapter 9

Limits Extraction

Prior to the derivation of the expected limits, we had to make sure their values are the most sensitive limits that our analysis can set. For that, we have done an optimization study finding the best cut value on the BDT discriminant with the idea to yield the lowest (the most sensitive) limit.

9.1 Optimization for the best limit

For this study, before doing the combination of electron and muon channels, we have optimized each of the channels separately. Systematical uncertainties were present only of the normalization type (lnN), since we are statistically limited and systematics plays a secondary role. As an example, for a specific analysis setup the 300 GeV fit in the muon channel yields the limit ('r-value') 255.25 (with the systematics but neglecting BBB uncertainties), without systematics the 'r-value' is 238.25. The difference is 17 parts in 255.25, which is just 6.7 %.

As can be seen from the plots 9.1 and 9.2, for high mass region the best cut to use is 0.99 for both electron and muon channels. For low mass region, the situation is more complicated. Depending on the mass point (and channel!) one cut is better than the other. For electron channel for 400 and 450 GeV mass points the best cut

Table 9.1: Suboptimal BDT cuts used in the analysis

channel	260 and 270 GeV	300 and 350 GeV	400 and 450 GeV	600 GeV to 1000 GeV
muons	0.1	0.7	0.7	0.99
electrons	0.4	0.4	0.925	0.99

is 0.925. In the lower region, the situation changes, 0.2 for 260 GeV, 0.4 for 270 and 300 GeV, 0.825 for 350 GeV.

Running the whole analysis for each separate cut and channel and spin hypothesis is not possible computationally taking into account the number of samples and shapes one has to create and process. That is why a reasonable compromise is to observe that for 260 $\rightarrow$ 350 GeV included, the suboptimal cut can be 0.4, being well inside the 1σ error band. This leaves the whole mass range with just three different cut values. This approach of suboptimal cuts, cuts which are close the best values but, most importantly, can be shared among several mass points, is what we adopted for this measurement.

For instance, for muons the best cuts are: 0.1 for 260 and 270 GeV, 0.5 for 300 GeV, 0.7 for 350 GeV, 0.925 for 400 and 450 GeV. Taking the approach of suboptimal cuts, the values we kept are: 0.1 for 260 and 270 GeV, 0.7 for 300 $\rightarrow$ 450 GeV included. This way we simplify the analysis to three different BDT cuts per channel and, at the same time, remain optimal within the error bands with respect to the best cut values. This is summarized in the Table 9.1.

9.2 Results from the fit

The extraction of the results is performed by what is called at CMS "Binned shape analysis". We used Higgs Combination Tool ("HiggsCombine") [68], which is a framework with the help of which the Higgs boson had been discovered. HiggsCombine is based on the RooStats package that has been very popular in the HEP community for years.

We do a simultaneous fit ($\tilde{M}_T$(HH) transverse mass distribution is used) of all three regions: signal region and two control regions, to extract both signal strength parameter as well as normalizations of $t\bar{t}$ and Drell-Yan backgrounds. We use the following command to produce expected limits with the Asimov [67] toy dataset :
combine -M Asymptotic -t -1 -v 3 -m massValue –run blind comb_card_massValue.txt.

The results in the Table 9.2 are final limits produced with the combined data of electron and muon channels. The corresponding plots, from which these numbers were extracted, are shown on the Figs. 9.3.

Full postfit distributions (the naming emphasises that all regions are used in the fit, signal region included) are shown on the Figs. 5.4 for the graviton case and Figs. 5.5 for the radion case.

Table 9.2: The expected and observed HH production cross section upper limits at 95% CL for different narrow resonance graviton (top) and radion (bottom) mass hypotheses for both dielectron and dimuon channels combined.

Mass, GeV	Observed Limit, pb	Expected Limit, pb
250	253.5	589.1
260	272.2	585.9
270	274.4	537.5
300	380.0	434.4
350	330.6	309.4
400	90.4	119.9
450	59.8	63.3
500	31.0	36.6
550	14.5	20.2
600	9.8	12.7
650	18.5	11.1
700	16.1	10.1
750	13.7	8.8
800	10.1	6.5
900	8.1	4.8
1000	5.8	4.2

Mass, GeV	Observed Limit, pb	Expected Limit, pb
250	107.3	297.7
260	170.8	410.9
270	207.0	470.3
300	451.7	496.9
350	532.6	496.9
400	155.7	171.1
450	89.3	82.0
500	36.0	54.4
550	18.7	28.5
600	13.2	19.6
650	24.6	17.2
700	16.4	12.0
750	13.9	10.4
800	12.6	9.8
900	6.9	5.6
1000	5.7	4.5

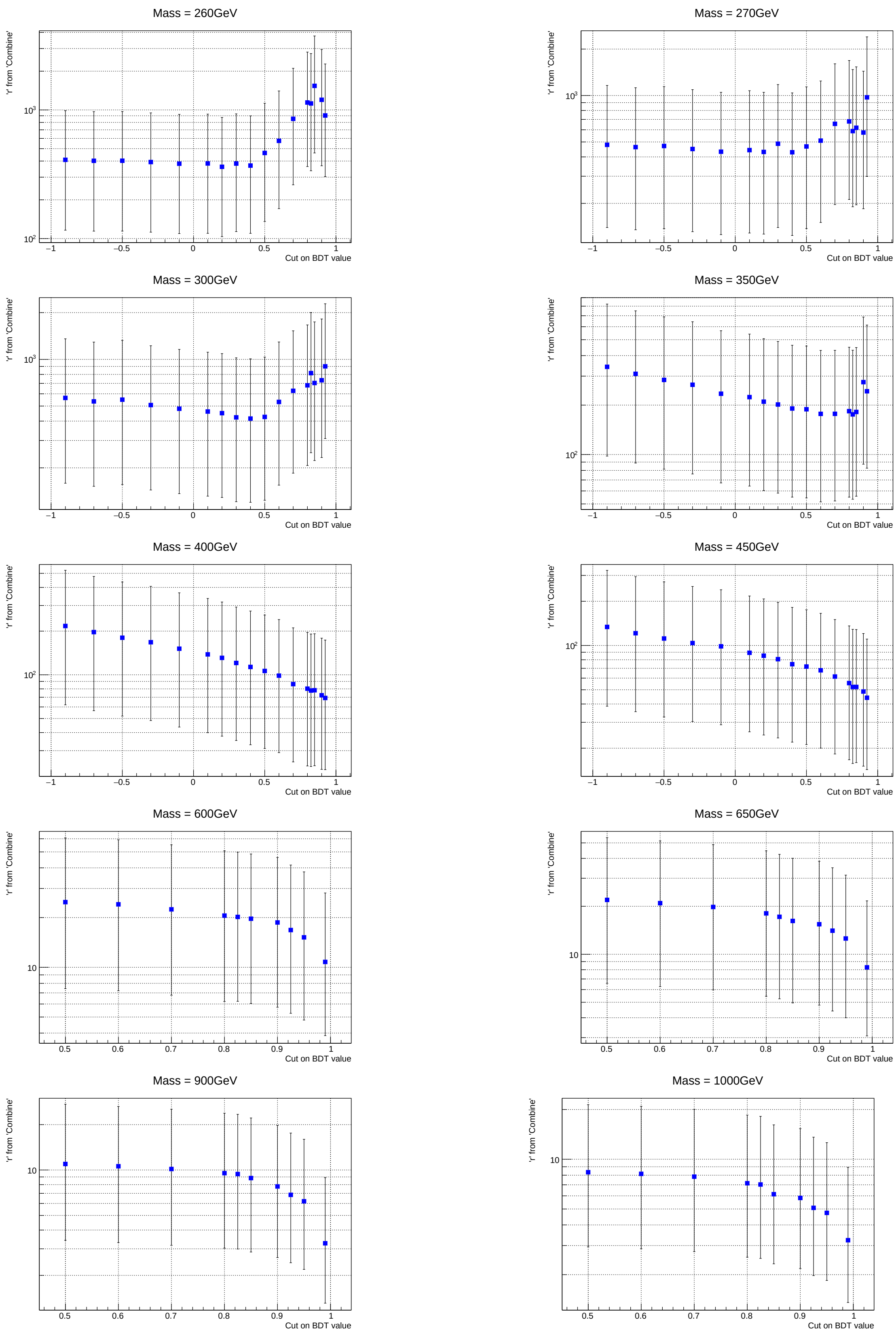

Figure 9.1: Cut on the BDT output vs 'r-value' from Combine. Electron channel.

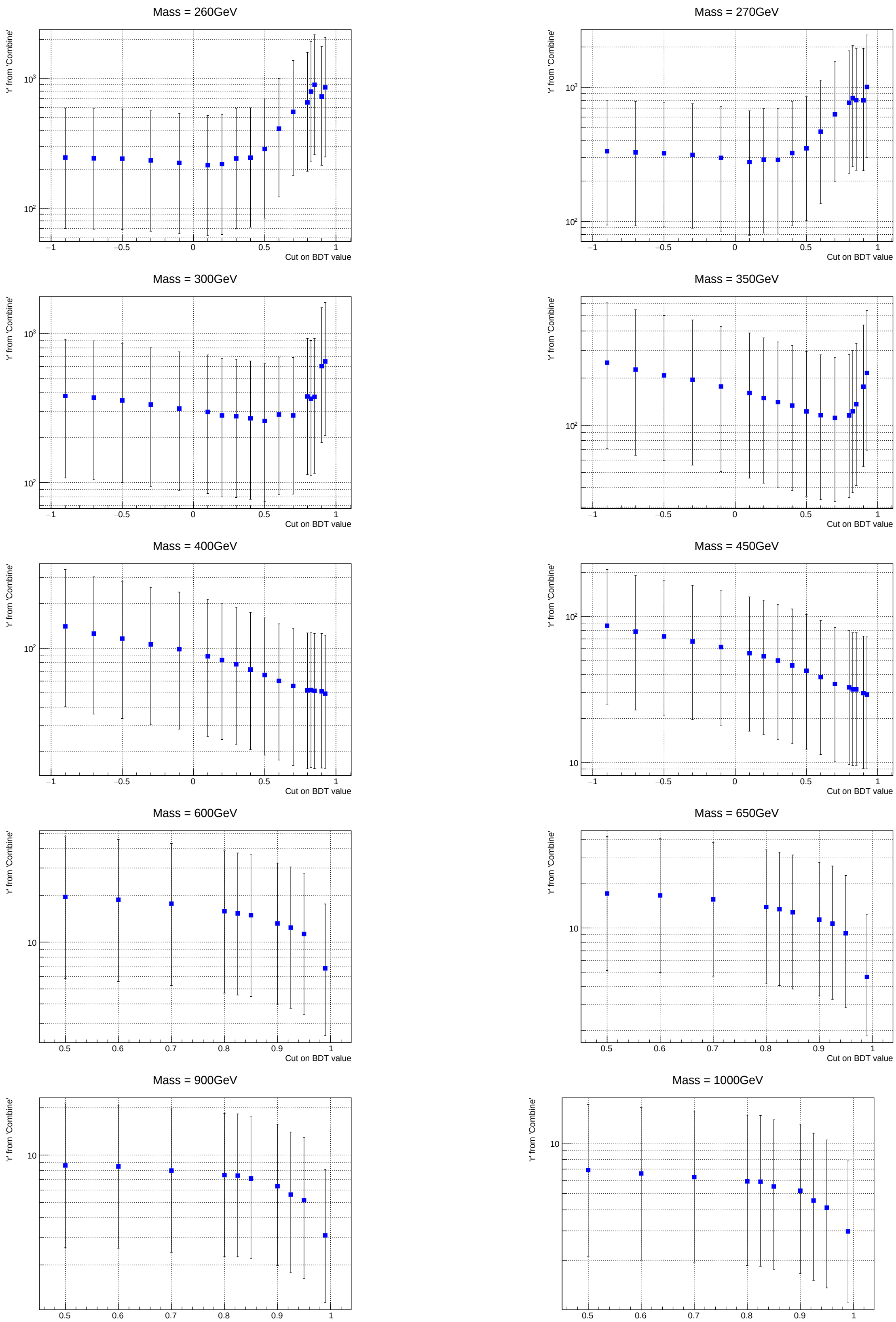

Figure 9.2: Cut on the BDT output vs 'r-value' from Combine. Muon channel.

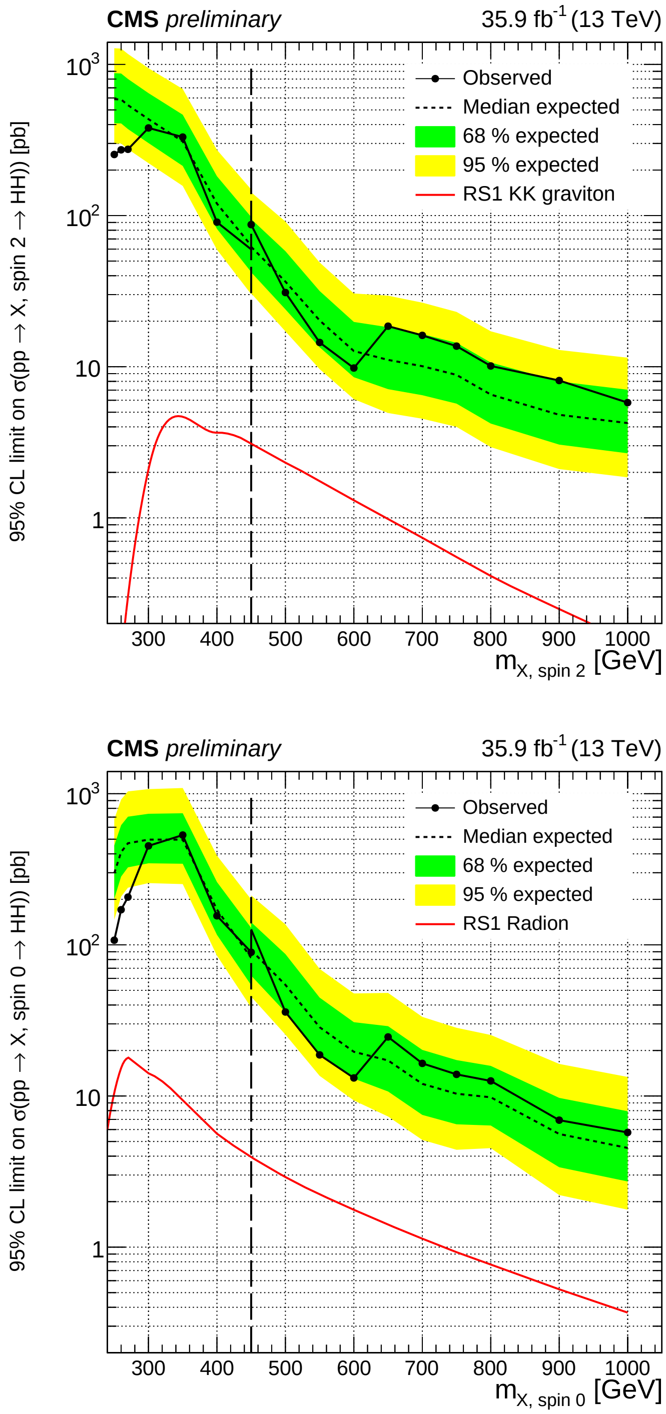

Figure 9.3: Expected (dashed line) and observed (solid line) limits on the cross section of a resonant HH production as a function of the mass of the narrow resonance for both leptonic channels combined. Graviton case is shown at the top and radion case at the bottom. The red line shows a theoretical prediction for the production of a WED particle with certain model assumptions [2].

Chapter *10*

$bbZZ$ measurements and combination of all HH channels

Even for the HL-LHC with almost $3\,\mathrm{ab}^{-1}$ of data, none of the HH analyses can reach the discovery sensitivity, thus the goal for all HH analyses now and in the nearest future is to contribute to the grand combination and only in this collaborative way to achieve the desired sensitivity. From the recent results of the HL-LHC HH combination projection analysis [69]: "the statistical combination of the five decay channels results in an expected significance for the standard model HH signal of 2.6σ". This is a clear sign that more data are needed. However, many Higgs analysts would agree that new statistical and MVA tools should be developed/employed. Thus, the next iteration of this analysis will most likely use a sophisticated neural network not only for the signal-background separation, but also for lepton reconstruction, etc.

This analysis is the search for the double Higgs boson production mediated by the intermediate graviton (and separately) by the radion in the bbZZ channel with the 2 b jets, 2 leptons, 2 neutrinos final state with the $35.9fb^{-1}$ 2016 dataset. According to the CMS Physics Coordination, for the paper in PRD this analysis has to be combined with the other $bbZZ$ analysis, which is focused on the 2 bjets, 2 leptons, 2 jets signature. The mass range to be covered in the combined measurement is also from 250 GeV to 1000 GeV.

Regarding the latest grand combination for the spin 0 and spin 2 cases [70] shown at the Fig. 10.1, the results are obtained for the extended mass range going from 250 GeV up to 3000 GeV, but no significant excess is found. The combination is done for the mass regions where at least two decay channels could contribute. Overall, $b\bar{b}\gamma\gamma$ is the most sensitive channel in the low mass region and $b\bar{b}b\bar{b}$ in the higher mass region (above $\sim$500 GeV).

This concludes the discussion of analysis details and in the next chapter we will summarise the main ideas that have been covered throughout this thesis.

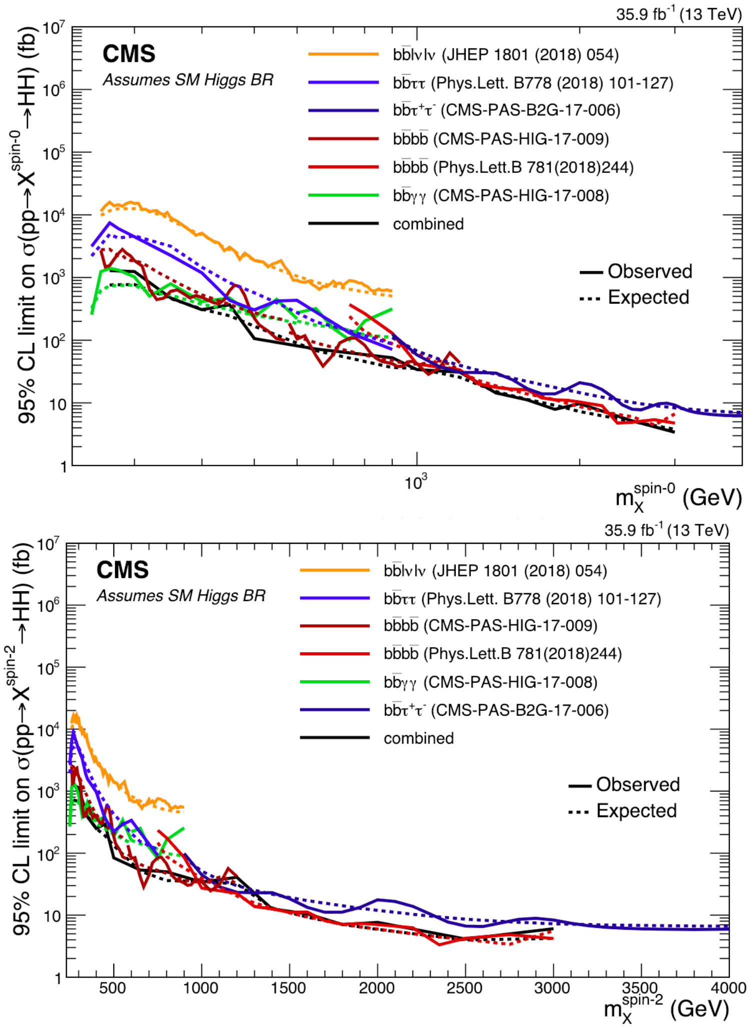

Figure 10.1: Combination of HH channels using 2016 data. Expected (dashed) and observed (solid line) 95% CL exclusion limits are shown. The results describe the production cross section of a narrow width spin 0 (top) and spin 2 (bottom) resonance decaying into a pair of SM Higgs bosons.

References

[1] Michele de Gruttola, Caterina Vernieri, Pierluigi Bortignon, David Curry, Ivan Furic, Jacobo Konigsberg, Sean-Jiun Wang, Paolo Azzurri, Tommaso Boccali, Andrea Rizzi, Silvio Donato, Stephane Brunet Cooperstein , James Olsen, Christopher Palmer, Lorenzo Bianchini, Christoph Grab, Gael Ludovic Perrin, and Luca Perrozzi. Search for the Standard Model Higgs Boson Produced in Association with W and Z and Decaying to Bottom Quarks. `http://cms.cern.ch/iCMS/jsp/db_notes/noteInfo.jsp?cmsnoteid=CMS%20AN-2015/168`.

[2] Alexandra Oliveira. Gravity particles from Warped Extra Dimensions, predictions for LHC. 2014.

[3] CMS Luminosity Measurements for the 2016 Data Taking Period. Technical Report CMS-PAS-LUM-17-001, CERN, Geneva, 2017.

[4] Serguei Chatrchyan et al. Observation of a new boson at a mass of 125 GeV with the CMS experiment at the LHC. *Phys. Lett.*, B716:30–61, 2012.

[5] Georges Aad et al. Observation of a new particle in the search for the Standard Model Higgs boson with the ATLAS detector at the LHC. *Phys. Lett.*, B716:1–29, 2012.

[6] Abdus Salam and John Clive Ward. On a gauge theory of elementary interactions. *Nuovo Cim.*, 19:165–170, 1961.

[7] S.L. Glashow. Partial symmetries of weak interactions. *Nucl.Phys.*, 22:579–588, 1961.

[8] Steven Weinberg. A model of leptons. *Phys.Rev.Lett.*, 19:1264–1266, 1967.

[9] Giuliano Panico. Prospects for double Higgs production. *Frascati Phys. Ser.*, 61:102, 2016.

[10] Matthew J. Dolan, Christoph Englert, and Michael Spannowsky. New Physics in LHC Higgs boson pair production. *Phys. Rev.*, D87(5):055002, 2013.

[11] Peisi Huang, Aniket Joglekar, Min Li, and Carlos E. M. Wagner. Corrections to Di-Higgs Production with Light Stops and Modified Higgs Couplings. 2017.

[12] Shinya Kanemura, Kunio Kaneta, Naoki Machida, Shinya Odori, and Tetsuo Shindou. Single and double production of the Higgs boson at hadron and lepton colliders in minimal composite Higgs models. *Phys. Rev.*, D94(1):015028, 2016.

[13] Lisa Randall and Raman Sundrum. Large mass hierarchy from a small extra dimension. *Phys. Rev. Lett.*, 83:3370–3373, Oct 1999.

[14] Kaustubh Agashe, Hooman Davoudiasl, Gilad Perez, and Amarjit Soni. Warped Gravitons at the LHC and Beyond. *Phys. Rev.*, D76:036006, 2007.

[15] A. Liam Fitzpatrick, Jared Kaplan, Lisa Randall, and Lian-Tao Wang. Searching for the Kaluza-Klein Graviton in Bulk RS Models. *JHEP*, 09:013, 2007.

[16] Oleg Antipin, David Atwood, and Amarjit Soni. Search for RS gravitons via W(L)W(L) decays. *Phys. Lett.*, B666:155–161, 2008.

[17] Albert M Sirunyan et al. Evidence for the Higgs boson decay to a bottom quark-antiquark pair. 2017.

[18] Aruna Kumar Nayak. Reconstruction of physics objects in the CMS detector. *PoS*, CHARGED2012:010, 2012.

[19] Albert M Sirunyan et al. Particle-flow reconstruction and global event description with the CMS detector. *JINST*, 12(10):P10003, 2017.

[20] CMS BTV POG. Supported Algorithms and Operating Points. `https://twiki.cern.ch/twiki/bin/viewauth/CMS/BtagRecommendation80XReReco#Supported_Algorithms_and_Operati`.

[21] J. Alwall, R. Frederix, S. Frixione, V. Hirschi, F. Maltoni, O. Mattelaer, H. S. Shao, T. Stelzer, P. Torrielli, and M. Zaro. The automated computation of tree-level and next-to-leading order differential cross sections, and their matching to parton shower simulations. *JHEP*, 07:079, 2014.

[22] SM Higgs Branching Ratios and Total Decay Widths (update in CERN Report4 2016). https://twiki.cern.ch/twiki/bin/view/LHCPhysics/CERNYellowReportPageBR#Higgs_2_g

[23] Stefano Frixione, Paolo Nason, and Giovanni Ridolfi. A Positive-weight next-to-leading-order Monte Carlo for heavy flavour hadroproduction. *JHEP*, 09:126, 2007.

[24] Rikkert Frederix, Emanuele Re, and Paolo Torrielli. Single-top t-channel hadroproduction in the four-flavour scheme with POWHEG and aMC@NLO. *JHEP*, 09:130, 2012.

[25] Simone Alioli, Paolo Nason, Carlo Oleari, and Emanuele Re. NLO single-top production matched with shower in POWHEG: s- and t-channel contributions. *JHEP*, 09:111, 2009. [Erratum: JHEP02,011(2010)].

[26] Johan Alwall et al. Comparative study of various algorithms for the merging of parton showers and matrix elements in hadronic collisions. *Eur. Phys. J. C*, 53:473–500, 2008.

[27] Ryan Gavin, Ye Li, Frank Petriello, and Seth Quackenbush. FEWZ 2.0: A code for hadronic Z production at next-to-next-to-leading order. *Comput. Phys. Commun.*, 182:2388, 2011.

[28] Ye Li and Frank Petriello. Combining QCD and electroweak corrections to dilepton production in FEWZ. *Phys. Rev. D*, 86:094034, 2012.

[29] Ryan Gavin, Ye Li, Frank Petriello, and Seth Quackenbush. W Physics at the LHC with FEWZ 2.1. *Comput. Phys. Commun.*, 184:208, 2013.

[30] k-factor for DY/Z. https://twiki.cern.ch/twiki/bin/viewauth/CMS/SummaryTable1G25ns#I

[31] Torbjorn Sjostrand, Stephen Mrenna, and Peter Z. Skands. A Brief Introduction to PYTHIA 8.1. *Comput. Phys. Commun.*, 178:852–867, 2008.

[32] J. Alwall, R. Frederix, S. Frixione, V. Hirschi, F. Maltoni, O. Mattelaer, H. S. Shao, T. Stelzer, P. Torrielli, and M. Zaro. The automated computation of tree-level and next-to-leading order differential cross sections, and their matching to parton shower simulations. *JHEP*, 07:079, 2014.

[33] Rikkert Frederix and Stefano Frixione. Merging meets matching in MC@NLO. *JHEP*, 12:061, 2012.

[34] John M. Campbell and R. K. Ellis. MCFM for the Tevatron and the LHC. *Nucl. Phys. Proc. Suppl.*, 205-206:10, 2010.

[35] Vardan Khachatryan et al. Event generator tunes obtained from underlying event and multiparton scattering measurements. *Eur. Phys. J. C*, 76(3):155, 2016.

[36] S. Agostinelli et al. GEANT4—a simulation toolkit. *Nucl. Instrum. Meth. A*, 506:250, 2003.

[37] The LHC Higgs cross-section working group. https://twiki.cern.ch/twiki/bin/view/LHCPhysics/LHCHXSWG.

[38] SM Higgs production cross sections at sqrt(s) = 13 TeV. https://twiki.cern.ch/twiki/bin/view/LHCPhysics/CERNYellowReportPageAt13TeV#ZHllH

[39] NNLO+NNLL top-quark-pair cross sections. https://twiki.cern.ch/twiki/bin/view/LHCPhysics/TtbarNNLO#Top_quark_pair_cross_se

[40] Single Top Cross sections. https://twiki.cern.ch/twiki/bin/viewauth/CMS/SingleTopSigma.

[41] CMS GEN XSEC Task Force. https://twiki.cern.ch/twiki/bin/viewauth/CMS/GenXsecTaskF

[42] Vardan Khachatryan et al. Performance of Electron Reconstruction and Selection with the CMS Detector in Proton-Proton Collisions at $\sqrt{s} = 8$ TeV. *JINST*, 10(06):P06005, 2015.

[43] Wolfgang Adam, R Fruhwirth, Are Strandlie, and T Todor. Reconstruction of Electrons with the Gaussian-Sum Filter in the CMS Tracker at the LHC. Technical Report CMS-NOTE-2005-001, CERN, Geneva, Jan 2005.

[44] Performance of muon identification in pp collisions at s**0.5 = 7 TeV. Technical Report CMS-PAS-MUO-10-002, CERN, Geneva, 2010.

[45] Serguei Chatrchyan et al. Performance of CMS muon reconstruction in *pp* collision events at $\sqrt{s} = 7$ TeV. *JINST*, 7:P10002, 2012.

[46] Thomas Lenzi. Development and Study of Different Muon Track Reconstruction Algorithms for the Level-1 Trigger for the CMS Muon Upgrade with GEM Detectors. Master's thesis, U. Brussels (main), 2013.

[47] CMS Muon POG. Reference muon id, isolation and trigger efficiencies for Run-II. `https://twiki.cern.ch/twiki/bin/viewauth/CMS/MuonReferenceEffsRun2`.

[48] CMS COLLABORATION. Particle–flow event reconstruction in CMS and performance for jets, taus, and E_T^{miss}. CMS Physics Analysis Summary CMS-PAS-PFT-09-001, CERN, 2009.

[49] CMS COLLABORATION. Commissioning of the particle-flow event reconstruction with the first lhc collisions recorded in the cms detector. CMS Physics Analysis Summary CMS-PAS-PFT-10-001, CERN, 2010.

[50] Matteo Cacciari and Gavin P. Salam. Dispelling the N^3 myth for the k_t jet-finder. *Phys. Lett. B*, 641:57, 2006.

[51] Matteo Cacciari, Gavin P. Salam, and Gregory Soyez. The anti-k_t jet clustering algorithm. *JHEP*, 04:063, 2008.

[52] CMS JetMET group. Jet Energy Resolution. `https://twiki.cern.ch/twiki/bin/viewauth/CMS/JetResolution`.

[53] The CMS collaboration. Missing transverse energy performance of the cms detector. *Journal of Instrumentation*, 6(09):P09001, 2011.

[54] CMS MET group. MET Corrections and Uncertainties for Run-II. https://twiki.cern.ch/twiki/bin/viewauth/CMS/MissingETRun2Corrections.

[55] CMS MET group. MET Filter Recommendations for Run II. https://twiki.cern.ch/twiki/bin/view/CMS/MissingETOptionalFiltersRun2.

[56] CMS Higgs WG. Binned shape analysis with the Higgs Combination Tool. https://twiki.cern.ch/twiki/bin/view/CMS/SWGuideHiggsAnalysisCombinedLimit#Binned_shape_analysis.

[57] bbbb team. Search for resonant pair production of Higgs bosons decaying to bottom quark-antiquark pairs in proton-proton collisions at 13 TeV. http://cms.cern.ch/iCMS/analysisadmin/get?analysis=HIG-17-009-pas-v5.pdf.

[58] Michele de Gruttola, Rami Kamalieddin, Ilya Kravchenko, Lesya Shchutska. Search for resonant diHiggs production with bbZZ decays with the 2b2l2nu signature using 35.9/fb data of 2016 pp collisions at the LHC. http://cms.cern.ch/iCMS/jsp/openfile.jsp?tp=draft&files=AN2017_198_v17.pdf.

[59] Chris Palmer. VHbb Electron Trigger and ID+ISO SFs for 2016 data. https://indico.cern.ch/event/604949/contributions/2543520/attachments/1439974/2216426/VHbb_TnP_SFs_egamma_april.pdf#search=vhbb%20AND%20cerntaxonomy%3A%22Indico%2FExperiments%2FCMS%20meetings%2FPH%20%2D%20Physics%2FEgamma%22.

[60] Gael L. Perrin, Pedro Fernandez Manteca. Muon Identification and Isolation Scale-Factors on 2016 Dataset. https://indico.cern.ch/event/611558/

contributions/2465881/attachments/1407735/2151747/TnP_06_02_2017.pdf.

[61] CMS Muon POG. Tracking SFs on the full 2016 data. https://twiki.cern.ch/twiki/bin/view/CMS/MuonWorkInProgressAndPagResults#Results_on_the_full_2016_data.

[62] Gael L. Perrin. Double Muon trigger efficiency per-leg approach. https://indico.cern.ch/event/636555/contributions/2577291/attachments/1453162/2241537/TnP_DoubleMuSF_03_05_17.pdf.

[63] Helge Voss, Andreas Höcker, Jörg Stelzer, and Frerik Tegenfeldt. TMVA, the toolkit for multivariate data analysis with ROOT. In *XIth International Workshop on Advanced Computing and Analysis Techniq ues in Physics Research (ACAT)*, page 40, 2007.

[64] Thomas Junk. Confidence level computation for combining searches with small statistics. *Nucl.Instrum.Meth.*, A434:435, 1999.

[65] A. L. Read. Presentation of search results: the CLs technique. *J. Phys. G: Nucl. Part. Phys.*, 28, 2002.

[66] SM Higgs Combination. Technical Report CMS-PAS-HIG-11-011, CERN, Geneva, 2011.

[67] Glen Cowan, Kyle Cranmer, Eilam Gross, and Ofer Vitells. Asymptotic formulae for likelihood-based tests of new physics. *Eur. Phys. J.*, C71:1554, 2011. [Erratum: Eur. Phys. J.C73,2501(2013)].

[68] CMS Higgs WG. Documentation of the RooStats -based statistics tools for Higgs PAG. https://twiki.cern.ch/twiki/bin/view/CMS/SWGuideHiggsAnalysisCombinedLimit.

[69] Prospects for HH measurements at the HL-LHC. Technical Report CMS-PAS-FTR-18-019, CERN, Geneva, 2018.

[70] Combination of searches for Higgs boson pair production in proton-proton collisions at $\sqrt{s} = 13$ TeV. Technical Report CMS-PAS-HIG-17-030, CERN, Geneva, 2018.

[71] S. Frixione, P. Nason, and C. Oleari. Matching nlo qcd computations with parton shower simulations: the powheg method. *JHEP*, 11:070, 2007.

[72] Gionata Luisoni, Paolo Nason, Carlo Oleari, and Francesco Tramontano. $HW^{\pm}$/HZ + 0 and 1 jet at NLO with the POWHEG BOX interfaced to GoSam and their merging within MiNLO. *JHEP*, 10:083, 2013.

[73] Comparison of nuisances for background only case, 350 GeV mass hypothesis. http://rkamalie.web.cern.ch/rkamalie/feb12/Comparison_of_nuisances_expectedSignal0_3

[74] Comparison of nuisances for s+b case, 350 GeV mass hypothesis. http://rkamalie.web.cern.ch/rkamalie/feb12/Comparison_of_nuisances_expectedSignal1_3

[75] Standard Model Cross Sections for CMS at 13 TeV. https://twiki.cern.ch/twiki/bin/viewauth/CMS/StandardModelCrossSectionsat13TeVInclusi

[76] Gunter Zech. Upper Limits in Experiments with Background Or Measurement Errors. *Nucl. Instrum. Meth.*, A277:608, 1989.

[77] Serguei Chatrchyan et al. Determination of jet energy calibration and transverse momentum resolution in CMS. *JINST*, 6:P11002, 2011.

[78] Emanuele Re. Single-top Wt-channel production matched with parton showers using the POWHEG method. *Eur. Phys. J.*, C71:1547, 2011.

[79] Grace Dupuis. Collider Constraints and Prospects of a Scalar Singlet Extension to Higgs Portal Dark Matter. *JHEP*, 07:008, 2016.

[80] CMS Higgs PAG. List of question for the preapproval checks. `https://twiki.cern.ch/twiki/bin/viewauth/CMS/HiggsWG/HiggsPAGPreapprovalChecks`.

[81] Albert M Sirunyan et al. Search for resonant and nonresonant Higgs boson pair production in the bblnulnu final state in proton-proton collisions at sqrt(s) = 13 TeV. 2017.

[82] Alexandra Oliveira. Gravity particles from Warped Extra Dimensions, predictions for LHC. 2014.

[83] I. Belotelov, I. Golutvin, D. Bourilkov, A. Lanyov, E. Rogalev, M. Savina, and S. Shmatov. Search for ADD extra dimensional gravity in di-muon channel with the CMS detector. CMS Note 2006/076, 2006.

[84] M. Aldaya, P. Arce, J. Caballero, B. de la Cruz, P. Garcia-Abia, J. M. Hernandez, M. I. Josa, and E. Ruiz. Discovery potential and search strategy for the standard model Higgs boson in the $H \to ZZ^{\star} \to 4\mu$ decay channel using a mass-independent analysis. CMS Note 2006/106, 2006.

[85] A. Brandt et al. Measurements of single diffraction at $\sqrt{s} = 630$ GeV: Evidence for a non-linear $\alpha(t)$ of the pomeron. *Nucl. Phys. B*, 514:3, 1998.

[86] W. Buchmüller and D. Wyler. Constraints on SU(5)-type leptoquarks. *Phys. Lett. B*, 177:377, 1986.

[87] CMS Collaboration. CMS technical design report, volume II: Physics performance. *J. Phys. G*, 34:995, 2007.

[88] CMS Collaboration. Jet performance in pp collisions at $\sqrt{s}$=7 TeV. CMS Physics Analysis Summary CMS-PAS-JME-10-003, 2010.

[89] S. Chatrchyan et al. The CMS experiment at the CERN LHC. *JINST*, 3:S08004, 2008.

[90] Particle Data Group, J. Beringer, et al. Review of Particle Physics. *Phys. Rev. D*, 86:010001, 2012.

[91] ALEPH, CDF, D0, DELPHI, L3, OPAL, SLD Collaborations, the LEP Electroweak Working Group, the Tevatron Electroweak Working Group, and the SLD Electroweak and Heavy Flavour Groups. Precision electroweak measurements and constraints on the Standard Model. 2010.

[92] I. Bertram, G. Landsberg, J. Linnemann, R. Partridge, M. Paterno, and H. B. Prosper. A recipe for the construction of confidence limits. Technical Report TM-2104, Fermilab, 2000.

[93] L. Moneta, K. Belasco, K. S. Cranmer, A. Lazzaro, D. Piparo, G. Schott, W. Verkerke, and M. Wolf. The RooStats Project. In *13th International Workshop on Advanced Computing and Analysis Techniques in Physics Research (ACAT2010)*. SISSA, 2010. PoS(ACAT2010)057.

[94] Vardan Khachatryan et al. Search for the standard model Higgs boson produced through vector boson fusion and decaying to $b\bar{b}$. *Phys. Rev.*, D92(3):032008, 2015.

[95] CMS Collaboration. Search for pair production of first-generation scalar leptoquarks in pp collisions at $\sqrt{s} = 7$ TeV. Submitted to *Phys. Rev. Lett.*, 2010.

[96] CMS Collaboration. Performance of cms muon reconstruction in pp collision events at $\sqrt{s} = 7$ TeV. Submitted to *J. Inst.*, 2012.

[97] ATLAS Collaboration. Search for the Higgs boson in the $H \rightarrow$WW(*)$\rightarrow \ell^+\nu\ell^-\bar{\nu}$ decay channel in pp collisions at $\sqrt{s} = 7$ TeV with the ATLAS detector. Submitted to *Phys. Rev. Lett.*, 2011.

[98] John M. Campbell, R. Keith Ellis, Paolo Nason, and Emanuele Re. Top-pair production and decay at NLO matched with parton showers. *JHEP*, 04:114, 2015.

[99] CMS EGM POG. Multivariate Electron Identification for Run2. `https://twiki.cern.ch/twiki/bin/viewauth/CMS/Multivari\ateElectronIdentificationRun2`.

[100] Torbjörn Sjöstrand, Stephen Mrenna, and Peter Skands. PYTHIA 6.4 physics and manual. *JHEP*, 05:026, 2006.

[101] C. Giunti and M. Laveder. Neutrino mixing. In F. Columbus and V. Krasnoholovets, editors, *Developments in Quantum Physics*. Nova Science Publishers, Inc., 2004.

[102] Richard Phillips Feynman, Robert Benjamin Leighton, and Matthew Sands. *The Feynman lectures on physics; New millennium ed.* Basic Books, New York, NY, 2010. Originally published 1963-1965.

[103] Savas Dimopoulos, Stuart Raby, and Frank Wilczek. Proton decay in supersymmetric models. *Physics Letters B*, 112(2):133 – 136, 1982.

[104] David J Griffiths. *Introduction to elementary particles; 2nd rev. version.* Physics textbook. Wiley, New York, NY, 2008.

[105] M. Della Negra, P. Jenni, and T. S. Virdee. Journey in the search for the higgs boson: The atlas and cms experiments at the large hadron collider. *Science*, 338(6114):1560–1568, 2012.

[106] Jennifer Ouellette. Einstein's quest for a unified theory. *APS*, 2015.

[107] E A Davis and Isabel Falconer. *J.J. Thompson and the discovery of the electron.* Taylor and Francis, Hoboken, NJ, 2002.

[108] Oreste Piccioni. *The Discovery of the Muon*, pages 143–162. Springer US, Boston, MA, 1996.

[109] G. Danby, J-M. Gaillard, K. Goulianos, L. M. Lederman, N. Mistry, M. Schwartz, and J. Steinberger. Observation of high-energy neutrino reactions and the existence of two kinds of neutrinos. *Phys. Rev. Lett.*, 9:36–44, Jul 1962.

[110] M. L. Perl, G. S. Abrams, and et al Boyarski. Evidence for anomalous lepton production in $e^+ - e^-$ annihilation. *Phys. Rev. Lett.*, 35:1489–1492, Dec 1975.

[111] K. Kodama et al. Observation of tau neutrino interactions. *Phys. Lett.*, B504:218–224, 2001.

[112] S. M. Bilenky. Neutrino in Standard Model and beyond. *Phys. Part. Nucl.*, 46(4):475–496, 2015.

[113] S Chandrasekhar. *Newton's principia for the common reader.* Oxford Univ., Oxford, 2003. The book can be consulted by contacting: PH-AID: Wallet, Lionel.

[114] Hanoch Gutfreund and Jurgen Renn. *The road to relativity: the history and meaning of Einstein's "The foundation of general relativity" : featuring the original manuscript of Einstein's masterpiece.* Princeton University Press, Princeton, NJ, Apr 2015.

[115] J. Butterworth. *Smashing Physics.* Headline Publishing Group, 2014.

[116] W N Cottingham and D A Greenwood. *An Introduction to the Standard Model of Particle Physics; 2nd ed.* Cambridge Univ. Press, Cambridge, 2007.

[117] Eric W. Weisstein. Fundamental forces.

[118] Carl Bender. Mathematical physics.

[119] Andrew Wayne. QED and the Men Who Made It: Dyson, Feynman, Schwinger, and Tomonaga by Silvan S. Schweber. *The British Journal for the Philosophy of Science*, 46(4):624–627, 1995.

[120] C. Patrignani et al. Review of Particle Physics. *Chin. Phys.*, C40(10):100001, 2016.

[121] Michelangelo L Mangano. Introduction to QCD. (CERN-OPEN-2000-255), 1999.

[122] Matt Strassler. Of particular significance: Conversations about science with theoretical physicist matt strassler.

[123] F. Englert and R. Brout. Broken symmetry and the mass of gauge vector mesons. *Phys. Rev. Lett.*, 13:321–323, Aug 1964.

[124] Peter W. Higgs. Broken symmetries and the masses of gauge bosons. *Phys. Rev. Lett.*, 13:508–509, Oct 1964.

[125] G. S. Guralnik, C. R. Hagen, and T. W. B. Kibble. Global conservation laws and massless particles. *Phys. Rev. Lett.*, 13:585–587, Nov 1964.

[126] Pauline Gagnon. *Who cares about particle physics? : making sense of the Higgs boson, the Large Hadron Collider and CERN.* Oxford University Press, 2016.

[127] Matthias U. Mozer. Electroweak Physics at the LHC. *Springer Tracts Mod. Phys.*, 267:1–115, 2016.

[128] Roger Wolf. *The Higgs Boson Discovery at the Large Hadron Collider*, volume 264. Springer, 2015.

[129] Steven Weinberg. The Making of the Standard Model. *Eur. Phys. J. C*, 34(hep-ph/0401010):5–13. 21 p. ; streaming video, 2003.

[130] Jose Andres Monroy Montanez, Kenneth Bloom, and Aaron Dominguez. Search for production of a Higgs boson and a single Top quark in multilepton final states in pp collisions at $\sqrt{s} = 13$ TeV, Jul 2018. Presented 23 Jul 2018.

[131] Albert M Sirunyan et al. Search for Higgs boson pair production in the $\gamma\gamma\mathrm{b}\overline{\mathrm{b}}$ final state in pp collisions at $\sqrt{s} = 13$ TeV. 2018.

[132] Lisa Randall and Raman Sundrum. A Large mass hierarchy from a small extra dimension. *Phys. Rev. Lett.*, 83:3370–3373, 1999.

[133] Kunihito Uzawa, Yoshiyuki Morisawa, and Shinji Mukohyama. Excitation of Kaluza-Klein gravitational mode. *Phys. Rev.*, D62:064011, 2000.

[134] H. Davoudiasl, J. L. Hewett, and T. G. Rizzo. Phenomenology of the Randall-Sundrum Gauge Hierarchy Model. *Phys. Rev. Lett.*, 84:2080, 2000.

[135] Michael Forger and Hartmann Romer. Currents and the energy momentum tensor in classical field theory: A Fresh look at an old problem. *Annals Phys.*, 309:306–389, 2004.

[136] Chuan-Ren Chen and Ian Low. Double take on new physics in double Higgs boson production. *Phys. Rev.*, D90(1):013018, 2014.

[137] Roberto Contino, Margherita Ghezzi, Mauro Moretti, Giuliano Panico, Fulvio Piccinini, and Andrea Wulzer. Anomalous Couplings in Double Higgs Production. *JHEP*, 08:154, 2012.

[138] Gennadi Sardanashvily. *Noether's theorems: applications in mechanics and field theory*. Atlantis studies in variational geometry. Springer, Paris, 2016.

[139] Thomas Schorner-Sadenius. *The Large Hadron Collider: harvest of run 1*. Springer, Cham, 2015.

[140] CERN. *Large Hadron Collider in the LEP Tunnel*, Geneva, 1984. CERN.

[141] Lyndon R Evans and Philip Bryant. LHC Machine. *JINST*, 3:S08001. 164 p, 2008. This report is an abridged version of the LHC Design Report (CERN-2004-003).

[142] Karsten Eggert, K Honkavaara, and Andreas Morsch. Luminosity considerations for the LHC. Technical Report CERN-AT-94-04-DI. CERN-LHC-Note-263. LHC-NOTE-263, CERN, Geneva, Feb 1994.

[143] Oswald Grobner. The LHC Vacuum System. (LHC-Project-Report-181. CERN-LHC-Project-Report-181):5 p, May 1998.